

1 **Technical Note: Nighttime OH and HO₂ chemical equilibria in the mesosphere – lower**
2 **thermosphere**

3 Mikhail Yu. Kulikov¹, Mikhail V. Belikovich¹, Aleksey G. Chubarov¹, Svetlana O. Dementyeva¹, and
4 Alexander M. Feigin¹

5 ¹A. V. Gaponov-Grekhov Institute of Applied Physics of the Russian Academy of Sciences, 46 Ulyanov
6 Str., 603950 Nizhny Novgorod, Russia

7 Correspondence to: Mikhail Yu. Kulikov (mikhail_kulikov@mail.ru)

8
9 **Abstract.** At the altitudes of the mesosphere – lower thermosphere OH and HO₂ play a significant
10 role in many physicochemical processes. Thus, monitoring their spatiotemporal evolution together with
11 other chemically active trace gases is one of the most important problems for this atmosphere region, in
12 which direct measurements are difficult. The paper studies the nighttime OH and HO₂ chemical equilibria
13 using the 3D chemical transport modeling within the general approach, which includes the identification
14 of the main sources and sinks in the equilibrium space-time areas and derivation of analytical criteria for
15 equilibrium validity. The presented analysis shows, that there are extended areas, where nighttime HO₂
16 and OH are close to their local equilibrium concentrations, determined mainly by the reaction between
17 HO_x – O_x components among themselves and with H₂O₂, N, NO, NO₂ and CO. In the upper mesosphere –
18 lower thermosphere the equilibrium expressions can be shortened, so that they include the HO_x – O_x
19 chemistry only. These expressions describe the HO₂ and OH equilibria from the top down to some
20 boundaries, the altitude positions of which vary in the interval between 72-73 and 85 km and depend
21 essentially on season and latitude. The developed analytical criteria almost everywhere reproduce well the
22 main features of these boundaries. Due to weak sensitivity to uncertainties of reaction rates and other
23 parameters, the criteria can be considered a robust instrument for HO₂ and OH equilibrium validation.
24 The obtained results allow us to extend previously proposed methods for the retrieval of poorly measured
25 components from measurement data and to develop new approaches.

27 **1 Introduction**

28 Monitoring the spatiotemporal evolution of chemically active trace gases is one of the most
29 important problems in atmospheric research. Despite the increase of the experimental data volume
30 nowadays, primarily due to the development in remote sensing methods, many important trace gases
31 continue to be unavailable for direct and regular measurements. A well-known way to increase the
32 information content of experimental campaigns is to use the available experimental data in conjunction
33 with a certain chemical or physicochemical model to derive unmeasured characteristics indirectly. Within
34 the framework of this approach, the model acts as *a priori* relationship between directly measured and
35 retrieved characteristics. The simplest model, that makes it possible to implement this approach, is based
36 on the condition of local (in both time and space) photochemical/chemical balance (local equilibrium)
37 between sources and sinks of the so-called “fast” components: trace gases with short lifetimes relatively,
38 in particular, to the characteristic transport times. Mathematically this condition does not mean that the
39 fast variables are at equilibrium, but when it is fulfilled, the corresponding concentrations are close to
40 their instantaneous equilibrium values. At the same time due to the strong dissipation in most cases
41 (except the special cases where the ensemble of fast components includes the slow family of these
42 components), there is no need to follow the law of matter conservation. It is possible to disregard
43 insignificant sinks and sources, including those caused by transport, in the corresponding balance
44 equations without the loss of accuracy. The resulting algebraic equations are the simplest *a priori* local
45 relations between measurable and retrieved trace gases. These relationships can be used to derive
46 information about hard-to-measure atmospheric species, determine key atmospheric characteristics (for
47 example, temperature (Marchand et al., 2007)), validate the data quality of simultaneous measurements of
48 several atmospheric components (Kulikov et al., 2018a), estimate reaction rate constants (Stedman et al.,
49 1975; Avallone and Toohey, 2001), evaluate sources/sinks (Cantrell et al., 2003), etc.

50 For several decades the photochemical/chemical equilibrium approximation has been used to solve
51 many atmospheric tasks. It is applied (see, e.g., the short review in Kulikov et al. (2018a) and references
52 therein) in investigations of the surface layer and free troposphere chemistry in different regions (over
53 megapolises, in rural areas, in the mountains, over the seas), in stratospheric chemistry studies, including
54 derivation of critical parameters in the ozone destruction catalytic cycles, and in studies of the HO_x – O_x
55 chemistry and airglows (O(¹S) green-line, O₂ A-band, OH Meinel band emissions) at the heights of the
56 mesosphere – lower thermosphere. In the latter case the distributions of unmeasured characteristics are
57 determined from the data of daytime and nighttime rocket and satellite measurements (e.g., Evans and
58 Llewellyn, 1973; Good, 1976; Pendleton et al., 1983; McDade et al., 1985; McDade and Llewellyn, 1988;
59 Evans et al., 1988; Thomas, 1990; Llewellyn et al., 1993; Llewellyn and McDade, 1996; Russell and
60 Lowe, 2003; Russell et al., 2005; Kulikov et al., 2006, 2009, 2017, 2022a, 2022b; Mlynczak et al., 2007,

61 2013a, 2013b, 2014, 2018; Smith et al., 2010; Xu et al., 2012; Siskind et al., 2008, 2015; Fytterer et al.,
62 2019) with the use of equilibrium assumptions for ozone and excited states of OH, O, and O₂. For
63 example, such an approach is applied to the data of the SABER (Sounding of the Atmosphere using
64 Broadband Emission Radiometry) instrument onboard the TIMED (Thermosphere Ionosphere
65 Mesosphere Energetics and Dynamics) satellite, which since 2002 continues to measure simultaneous
66 profiles of temperature, ozone and volume emission rates of OH* transitions in wide ranges of altitude,
67 local time and latitude with a rather high space-time resolution.

68 Note a number of general aspects of the application of equilibrium conditions in the above
69 examples. First of all, there are no clear criteria, indicating the conditions under which the use of
70 equilibrium approximation is justified. Usually a certain component is taken to be a fast variable, if its
71 lifetime is much shorter, than the lifetimes of other components of studied photochemical/chemical
72 system or the duration of a day, daytime, nighttime, etc. For example, in the papers on SABER data
73 processing (Mlynczak et al., 2013a, 2013b, 2014, 2018) it is assumed, that the nighttime ozone chemical
74 equilibrium in the mesopause is well fulfilled at altitudes of 80–100 km, since the nighttime ozone
75 lifetime at these altitudes varies in the range from several minutes to several tens of minutes. Note, that
76 this assumption is quite popular and used in different tasks (e.g., Swenson and Gardner, 1998; Marsh et
77 al., 2006; Smith et al., 2009; Nikoukar et al., 2007; Xu et al., 2010, 2012; Kowalewski et al., 2014;
78 Grygalashvyly et al., 2014; Grygalashvyly, 2015; Sonnemann et al., 2015; Kulikov et al., 2021).
79 Belikovich et al. (2018) and Kulikov et al. (2018b, 2019, 2023a) analyzed the nighttime ozone chemical
80 equilibrium numerically, analytically, and with the use of SABER/TIMED data. It was revealed, that the
81 short lifetime is not a sufficient condition, so, this equilibrium may be significantly disturbed above 80
82 km. The local ratio between true and equilibrium concentrations may vary widely and reach up to several
83 orders of magnitude (e.g., Figure 5 in Kulikov et al. (2018b)). Thus, without special restrictions the error
84 in retrieved characteristics due to the use of equilibrium approximation is uncontrollable and may
85 significantly exceed all other errors in the retrieval procedure due to, for example, uncertainties in the
86 measurement data and rate constants.

87 Since the papers of Belikovich et al. (2018) and Kulikov et al. (2018b, 2019, 2023a), we developed
88 the general approach to correctly identify fast components, employing the data from a global 3D chemical
89 transport model. It includes:

- 90 1. Plotting of the equilibrium space-time maps of the components of interest.
- 91 2. Identification of the main sources and sinks in the found equilibrium areas.
- 92 3. Derivation and subsequent use of analytical criteria that make it possible to determine the fulfillment of
93 the equilibrium condition locally (in time and space) with the use of the measurement data only.

94 The latter point is based on the theory of chemical equilibrium of a certain trace gas, acquired from
95 estimations of its lifetime and equilibrium concentration, and time dependences of these characteristics
96 (Kulikov et al., 2023a). Note, that when equilibrium condition is applied to measurement data in the
97 retrieval of unmeasured characteristics, the criterion allows controlling and limiting the possible error
98 caused by the equilibrium approximation.

99 The main goal of the paper is to apply this approach to the analysis of nighttime OH and HO₂
100 chemical equilibria in the mesosphere – lower thermosphere. Along with O and H, OH and HO₂ are
101 important components of HO_x – O_x chemistry, participating (a) in chemical heating through, in particular,
102 O+OH → O₂+H and O+HO₂ → O₂+OH exothermic reactions, (b) in formation of airglows, (c) in
103 catalytic cycles of the ozone destruction. Moreover, the equilibrium conditions of OH and HO₂ are
104 additional *a priori* relationships, that can be used to retrieve these components or other characteristics
105 from measured data. In particular, Panka et al. (2021) proposed the method for nighttime total OH
106 retrieval from SABER/TIMED data at 80-100 km, which does not use the ozone chemical equilibrium.
107 However, the method applies the equilibrium between sources and sinks not only to excited states of OH
108 with ultrashort lifetimes, but also to the ground state. Therefore, this point is verified in our paper.

109 In the next section we present the used model and methods. In Section 3 the model data are used to
110 plot HO₂ and OH equilibrium maps. In Sections 4-5 we identify the main reactions, determining
111 equilibria of these gases, and present their shortened equilibria conditions at the upper mesosphere and
112 lower thermosphere altitudes. In Section 6 the criteria for HO₂ and OH equilibria validity are developed.
113 In Section 7 we discuss the obtained results and their possible applications.

114

115 **2 Used 3D model and Approaches**

116 The analysis of OH and HO₂ nighttime chemical equilibria was carried out, using the data, obtained
117 with calculation of 3D chemical transport model of the middle atmosphere, developed at the Leibniz
118 Institute of Atmospheric Physics (e.g., Sonnemann et al., 1998; Körner & Sonnemann, 2001;
119 Grygalashvyly et al., 2009; Hartogh et al., 2004, 2011) to investigate the mesosphere – lower
120 thermosphere chemistry, in particular, in the extended mesopause region. A number of papers (e.g.,
121 Hartogh et al., 2004, 2011; Sonnemann, et al., 2006, 2008) validated the model with measurements, in
122 particular, for ozone and water vapor.

123 The space-time distribution of temperature and winds were taken from the model of the dynamics
124 of the middle atmosphere COMMA-IAP (e.g., Kremp et al., 1999; Berger and von Zahn, 1999) with an
125 updated frequency of 1 day and linear smoothing between subsequent updates to avoid unrealistic jumps

126 in the calculated concentrations of trace gases. 3D advective transport is taken into account with the use
 127 of the Walcek-scheme (Walcek, 2000). The vertical diffusive transport (turbulent and molecular) is
 128 calculated with the use of the implicit Thomas algorithm (Morton and Mayers, 1994). The model grid has
 129 118 pressure-height levels (0–135 km), 16 latitudinal and 32 longitudinal levels. The chemical module
 130 (see Table 1) comprises 25 constituents (O, O(¹D), O₃, H, OH, HO₂, H₂O₂, H₂O, H₂, N, NO, NO₂, NO₃,
 131 N₂O, CH₄, CH₂, CH₃, CH₃O₂, CH₃O, CH₂O, CHO, CO, CO₂, O₂, N₂), 54 chemical reactions between
 132 them and 15 photo-dissociation reactions. The model utilizes the pre-calculated dissociation rates (Kremp
 133 et al., 1999) and their dependence on the altitude and solar zenith angle.

134 The model was used to calculate a one-year global evolution of the above mentioned trace gases. To
 135 remove the transition regions corresponding to sunset and sunrise, we use only local times when the solar
 136 zenith angle $\chi > 105^\circ$. As a result, we find the spatiotemporal series of the OH/OH^{eq} and HO_2/HO_2^{eq}
 137 ratios. Here OH and HO_2 are the local nighttime values of hydroxyl and hydroperoxyl radicals, calculated
 138 by the model, OH^{eq} and HO_2^{eq} are their local equilibrium values, corresponding to the instantaneous
 139 balance between production and loss terms respectively. To determine each local value of OH^{eq} and
 140 HO_2^{eq} we used the local values of the parameters (temperature, O₂, and N₂) and the concentrations of
 141 other trace gases, determining local chemical sources and sinks of OH and HO_2 . Then the OH/OH^{eq} and
 142 HO_2/HO_2^{eq} series were averaged over the zonal coordinate and time during each month and were
 143 presented as height-latitude maps, depending on the month. Each map contains lines, marking the
 144 boundaries of the equilibrium areas, where the following conditions are satisfied:

$$145 \left\{ \begin{array}{l} |\langle OH/OH^{eq} \rangle - 1| \leq 0.1 \\ \sigma_{OH/OH^{eq}} \leq 0.1 \end{array} \right\}, \left\{ \begin{array}{l} |\langle HO_2/HO_2^{eq} \rangle - 1| \leq 0.1 \\ \sigma_{HO_2/HO_2^{eq}} \leq 0.1 \end{array} \right\}, \quad (1)$$

146 where the angle brackets are used to denote the values averaged in time and space, $\sigma_{OH/OH^{eq}}$ and
 147 $\sigma_{HO_2/HO_2^{eq}}$ are standard deviations of the OH/OH^{eq} and HO_2/HO_2^{eq} ratios from 1 respectively.

148 Then we plotted spatiotemporal maps, showing the relative contribution of each reaction to a
 149 summarized source or sink at all altitudes and latitudes. These maps helped us to identify the main
 150 sources and sinks, describing the chemical equilibrium of nighttime OH and HO₂ in the equilibrium areas
 151 to an accuracy of better than a few percent.

152 Finally, we obtained and verified the analytical criteria of OH and HO₂ nighttime chemical
 153 equilibria according to Kulikov et al. (2023a). The paper considered the pure chemical evolution of a
 154 certain trace gas n :

$$155 \frac{dn}{dt} = I_n - S_n = -\frac{1}{\tau_n}(n - n^{eq}),$$

156
$$\tau_n = \frac{n}{S_n}, \quad n^{eq} = \frac{n \cdot I_n}{S_n}, \quad (2)$$

157 where t is time, I_n and S_n are total photochemical/chemical sources and sinks of n respectively, τ_n is the
 158 n lifetime and n^{eq} is its equilibrium concentration, corresponding to the condition $I_n = S_n$. The lifetime
 159 determines the characteristic time scale, for which n approaches n^{eq} , when $n^{eq} = const$. In general case
 160 τ_n and n^{eq} are functions of time. Kulikov et al. (2023a) showed strictly mathematically, that the local
 161 values of n and n^{eq} are close to each other ($n(t) \approx n^{eq}(t)$), when $\tau_n \ll \tau_{n^{eq}}$, where $\tau_{n^{eq}}$ is the local time
 162 scale of n^{eq} :

163
$$\tau_{n^{eq}} \equiv \frac{n^{eq}}{|dn^{eq}/dt|}. \quad (3)$$

164 The expression for τ_n is found from the total sink of n . The expression for $\tau_{n^{eq}}$ is derived from Eq. (3)
 165 with the use of differential equations, describing chemical evolution of other reacting components, which
 166 determine the expression for n^{eq} . Kulikov et al. (2023a) also showed, when $\tau_n \ll \tau_{n^{eq}}$, $n \cong n^{eq} (1 -$
 167 $sign(\frac{dn^{eq}}{dt}) \cdot \frac{\tau_n}{\tau_{n^{eq}}})$ in the first order approximation. Thus, the criterion

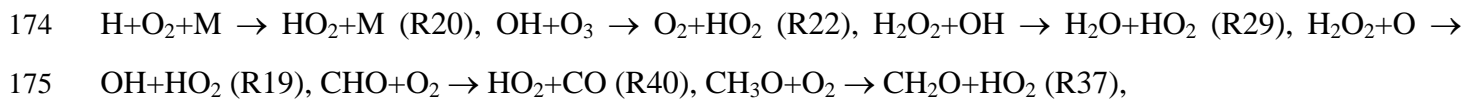
168
$$\tau_n / \tau_{n^{eq}} \leq 0.1 \quad (4)$$

169 is sufficient, in order to the possible relative difference between n and n^{eq} to be no more than 0.1.

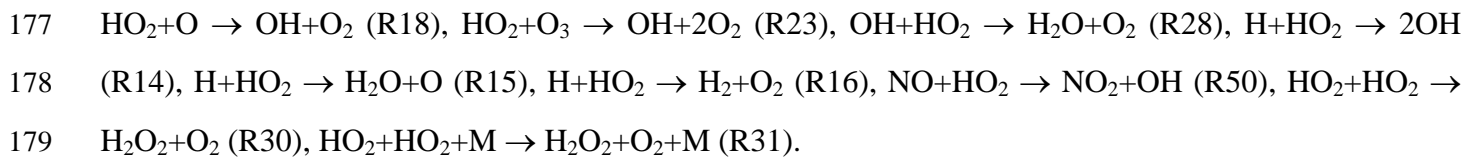
170

171 **3 Nighttime HO₂ and OH chemical equilibria**

172 According to the Table 1 HO₂ chemical sources in nighttime are determined by the following
 173 reactions:



176 whereas chemical sinks of this component are as follows:



180 Thus, HO₂ local equilibrium concentration is described by the following equation:

181
$$HO_2^{eq} = \frac{k_{20} \cdot H \cdot M \cdot O_2 + k_{22} \cdot OH \cdot O_3 + k_{29} \cdot H_2O_2 \cdot OH + k_{19} \cdot H_2O_2 \cdot O + k_{40} \cdot CHO \cdot O_2 + k_{37} \cdot CH_3O \cdot O_2}{k_{18} \cdot O + k_{23} \cdot O_3 + k_{28} \cdot OH + (k_{14} + k_{15} + k_{16}) \cdot H + k_{50} \cdot NO + 2 \cdot (k_{30} + k_{31} \cdot M) \cdot HO_2} \quad (5)$$

182 Figure 1 plots height-latitude cross sections for the $\langle HO_2/HO_2^{eq} \rangle$ ratio for each month. The
 183 black solid lines mark the boundaries of equilibrium areas, where according to condition (1) local values
 184 of HO_2 are close to their equilibrium values with a possible bias of less than 10%. At low and middle
 185 latitudes one can see the presence of the main equilibrium area, which extends from the top of the
 186 analyzed altitude range to the lower boundary. The height of this equilibrium boundary, $z_{HO_2^{eq}}$, depends
 187 on the season and latitude and varies in the interval between 73 and 85 km. It is the highest and the lowest
 188 during the summer and winter respectively at the middle latitudes. Near the equator $z_{HO_2^{eq}}$ demonstrates
 189 the weakest annual variations and varies in the 81-83 km range. There are local areas below the upper
 190 longest black line, but they are small and irregular and can be omitted from our consideration. Note that
 191 the maps show the existence of equilibrium near 50 km, which can be assumed to be the beginning of the
 192 main equilibrium area in the stratosphere. At high latitudes there is the main equilibrium area as at low
 193 and middle latitudes, but this area above 70-75° of latitude can extend down to 50 km.

194 In accordance to the Table 1 OH chemical sources are determined by the following reactions:

195 $H+O_3 \rightarrow OH+O_2$ (R21), $HO_2+O \rightarrow OH+O_2$ (R18), $HO_2+O_3 \rightarrow OH+2O_2$ (R23), $H+HO_2 \rightarrow 2OH$ (R14),
 196 $NO+HO_2 \rightarrow NO_2+OH$ (R50), $H_2O_2+O \rightarrow OH+HO_2$ (R19), $H+NO_2 \rightarrow OH+NO$ (R51), $O(^1D)+H_2O \rightarrow$
 197 $2OH$ (R7), $O(^1D)+H_2 \rightarrow H+OH$ (R8), $CH_4+O(^1D) \rightarrow CH_3+OH$ (R9),

198 whereas chemical sinks of this component are as follows:

199 $OH+O \rightarrow H+O_2$ (R17), $OH+O_3 \rightarrow O_2+HO_2$ (R22), $OH+HO_2 \rightarrow H_2O+O_2$ (R28), $OH+OH \rightarrow H_2O+O$
 200 (R26), $OH+OH+M \rightarrow H_2O_2+M$ (R27), $H+OH+N_2 \rightarrow H_2O+N_2$ (R24), $H_2O_2+OH \rightarrow H_2O+HO_2$ (R29),
 201 $OH+CO \rightarrow H+CO_2$ (R32), $CH_4+OH \rightarrow CH_3+H_2O$ (R33), $OH+H_2 \rightarrow H_2O+H$ (R25), $N+OH \rightarrow NO+H$
 202 (R49).

203 Thus, OH local equilibrium concentration is described by the following equation:

$$\begin{aligned}
 204 \quad OH^{eq} = & (k_{21} \cdot H \cdot O_3 + k_{18} \cdot O \cdot HO_2 + k_{23} \cdot HO_2 \cdot O_3 + 2 \cdot k_{14} \cdot H \cdot HO_2 + k_{50} \cdot HO_2 \cdot NO + k_{19} \cdot \\
 205 \quad & H_2O_2 \cdot O + k_{24} \cdot H \cdot N_2 + k_{51} \cdot NO_2 \cdot H + 2 \cdot k_7 \cdot O(^1D) \cdot H_2O + k_8 \cdot O(^1D) \cdot H_2 + k_9 \cdot O(^1D) \cdot \\
 206 \quad & CH_4) / (k_{17} \cdot O + k_{22} \cdot O_3 + k_{28} \cdot HO_2 + 2 \cdot (k_{26} + k_{27} \cdot M) \cdot OH + k_{29} \cdot H_2O_2 + k_{32} \cdot CO + k_{33} \cdot \\
 207 \quad & CH_4 + k_{25} \cdot H_2 + k_{25} \cdot N) \quad (6)
 \end{aligned}$$

208 Figure 2 shows height-latitude cross sections for the $\langle OH/OH^{eq} \rangle$ ratio for each month. In this
 209 case the equilibrium covers up to 70-80% of the presented ranges of heights and latitudes, so that the
 210 black solid lines mark the external boundaries of non-equilibrium areas. In March and September this
 211 area is almost symmetrical to the equator. In April-August it is shifted towards the northern hemisphere.
 212 In October-February this area is higher in the southern hemisphere. In all months it is below 85-86 km. In

213 the polar regions there are latitudinal ranges, where OH is close to equilibrium throughout the entire range
 214 of heights.

215

216 **4 The main reactions, determining HO₂ and OH equilibria**

217 Figure 3 presents height-latitude contour maps, showing the relative contribution of a certain
 218 reaction to the total source and sink of HO₂ in January, taken as an example. To increase the information
 219 content of the panels, the altitude range is cut off everywhere to 10⁻³ hPa, since there are no significant
 220 changes above. Note firstly, that reaction H+O₂+M → HO₂+M determines a major (up to 95% and more)
 221 contribution in the main equilibrium area almost everywhere, except for the polar regions above 70-75° of
 222 latitude and below 75-80 km, where the reactions OH+O₃ → O₂+HO₂ and H₂O₂+OH → H₂O+HO₂
 223 become important and should be taken into account. Other reactions (H₂O₂+O → OH+HO₂, CHO+O₂ →
 224 HO₂+CO, CH₃O+O₂ → CH₂O+HO₂) together contribute less than 2-3% to the total source of HO₂ in the
 225 main equilibrium area and may be omitted. Secondly, the reaction HO₂+O → OH+O₂ determines a major
 226 (up to 95% and more) contribution to the total sink in the main equilibrium area almost everywhere,
 227 except for the same small polar areas, as in the considered case with the sources, where the reactions
 228 HO₂+O₃ → OH+2O₂ and NO+HO₂ → NO₂+OH are important and should be taken into account. The
 229 reactions OH+HO₂ → H₂O+O₂, H+HO₂ → 2OH, H+HO₂ → H₂O+O, and H+HO₂ → H₂+O₂ contribute
 230 cumulatively up to 10-15% of the total sink near the boundary of the main equilibrium area. The
 231 remaining reactions (HO₂+HO₂ → H₂O₂+O₂, HO₂+HO₂+M → H₂O₂+O₂+M) are not important in the
 232 main equilibrium area and can be omitted.

233 Therefore, the expression for HO₂ local equilibrium concentration can be simplified as follows:

$$234 \text{HO}_2^{eq} = \frac{k_{20} \cdot H \cdot M \cdot O_2 + k_{22} \cdot OH \cdot O_3 + k_{29} \cdot H_2O_2 \cdot OH}{k_{18} \cdot O + k_{23} \cdot O_3 + k_{28} \cdot OH + (k_{14} + k_{15} + k_{16}) \cdot H + k_{50} \cdot NO} \quad (7)$$

235 Figure 4 presents height-latitude contour maps, showing the relative contribution of a certain
 236 reaction to the total source and sink of OH in January, taken as an example in Figure 3. As in the previous
 237 case, the altitude range is cut off at 10⁻³ hPa, because only the panels for the reactions H+O₃ → OH+O₂
 238 and HO₂+O → OH+O₂ consist of interesting variations above. Note, that firstly these reactions are the
 239 main OH sources in the upper part of the presented distributions down to 70-75 km, where they jointly
 240 provide up to a 95% contribution to the equilibrium concentration. Also the reaction HO₂+O₃ → OH+2O₂
 241 is major source in the lower part of the presented distribution from 50 to 60-70 km. The reaction
 242 NO+HO₂ → NO₂+OH is important around non-equilibrium areas of OH and should be taken into
 243 account, whereas the reaction H +NO₂ → OH+NO is important in compact altitude-latitude areas near the
 244 poles, the reaction H+HO₂ → 2OH gives up to 10-15% contribution in small areas near the equilibrium

245 boundary. Other reactions ($O(^1D)+H_2O \rightarrow 2OH$, $O(^1D)+H_2 \rightarrow H+OH$, $CH_4+O(^1D) \rightarrow CH_3+OH$, H_2O_2+O
 246 $\rightarrow OH+HO_2$) together contribute less than 2-3% of the total source of OH in the main equilibrium area
 247 and can be omitted. Secondly, the reaction $OH+O \rightarrow H+O_2$ is the main OH sink in the upper part of the
 248 presented distributions down to 70-80 km, where it provides up to 95% of the equilibrium concentration.
 249 The reactions $OH+CO \rightarrow H+CO_2$ and $OH+O_3 \rightarrow O_2+HO_2$ are major in the lower part of the presented
 250 distributions from 50 to 70-80 km. The reaction $OH+HO_2 \rightarrow H_2O+O_2$ is significant enough around non-
 251 equilibrium areas of OH, whereas the reaction $H_2O_2+OH \rightarrow H_2O+HO_2$ is important in the compact
 252 altitude-latitude area near the poles. Other reactions ($OH+OH \rightarrow H_2O+O$, $OH+H_2 \rightarrow H_2O+H$, $N+OH \rightarrow$
 253 $NO+H$, $CH_4+OH \rightarrow CH_3+H_2O$, $H+OH+N_2 \rightarrow H_2O+N_2$, $OH+OH+M \rightarrow H_2O_2+M$) together contribute
 254 less than 2-3% to the total sink of OH in the main equilibrium area and can be omitted.

255 Therefore, the expression for OH local equilibrium concentration can be simplified as follows:

$$256 \quad OH^{eq} = \frac{k_{21} \cdot H \cdot O_3 + k_{18} \cdot O \cdot HO_2 + k_{23} \cdot HO_2 \cdot O_3 + 2 \cdot k_{14} \cdot H \cdot HO_2 + k_{24} \cdot H \cdot N_2 + k_{50} \cdot HO_2 \cdot NO + k_{51} \cdot NO_2 \cdot H}{k_{17} \cdot O + k_{22} \cdot O_3 + k_{28} \cdot HO_2 + k_{29} \cdot H_2O_2 + k_{32} \cdot CO} \quad (8)$$

257

258 **5 Shortened equilibrium conditions of HO₂ and OH in the upper mesosphere and lower** 259 **thermosphere**

260 The above analysis revealed, that the reactions describing the equilibrium conditions (7-8) in the
 261 lower and middle mesosphere are different from those in the upper mesosphere and lower thermosphere.
 262 This means that the task of applying these conditions can be divided into two parts depending on the
 263 selected altitude range. At the upper mesosphere and lower thermosphere altitudes, we can consider only
 264 the HO_x – O_x chemistry, excluding the reactions with participation of H₂O₂, N, NO, NO₂, and CO. In
 265 addition, we can omit the reactions $HO_2+O_3 \rightarrow OH+2O_2$, $OH+O_3 \rightarrow O_2+HO_2$, and $OH+HO_2 \rightarrow H_2O+O_2$
 266 due to their insignificance here. As a result, the shortened equilibrium conditions of HO₂ and OH for this
 267 altitude range are as follows:

$$268 \quad HO_{2sh}^{eq} = \frac{k_{20} \cdot H \cdot M \cdot O_2}{k_{18} \cdot O + (k_{14} + k_{15} + k_{16}) \cdot H} \quad (9)$$

$$269 \quad OH_{sh}^{eq} = \frac{k_{21} \cdot H \cdot O_3 + k_{18} \cdot O \cdot HO_2 + 2 \cdot k_{14} \cdot H \cdot HO_2}{k_{17} \cdot O} \quad (10)$$

270 Figure 5 shows height-latitude cross sections for the $\langle HO_2/HO_{2sh}^{eq} \rangle$ ratio for each month. In each
 271 panel the upper longest black line marks the lower boundary of the main equilibrium area, where
 272 according to condition (1) $HO_2 \approx HO_{2sh}^{eq}$ with possible bias of less than 10%. As in the case of Figure 1,
 273 this area extends from the top of the analyzed altitude range. There are also very small equilibrium areas
 274 below, which can be omitted from our consideration. The height of the lower boundary of the main

275 equilibrium area, $z_{HO_2_{sh}^{eq}}$, depends essentially on the season and latitude. Comparing with Figure 1 one can
 276 see, that it reproduces many features of $z_{HO_2_{sh}^{eq}}$ at low and middle latitudes. In particular, $z_{HO_2_{sh}^{eq}}$ varies in
 277 the interval between 73 and 85 km, as in the case of $z_{HO_2^{eq}}$. In the middle latitudes $z_{HO_2_{sh}^{eq}}$ in summer is
 278 several km higher than in winter. Near the equator $z_{HO_2_{sh}^{eq}}$ demonstrates the weakest annual variations and
 279 varies in the range of 81-83 km. So, one can conclude, that the exclusion of a number of reactions does
 280 not lead to significant changes in the space-time distributions of the HO₂ equilibrium.

281 Figure 6 plots height-latitude cross sections for the $\langle OH/OH_{sh}^{eq} \rangle$ ratio for each month. As in the
 282 previous case, this is the lower boundary of the equilibrium area, where according to condition (1)
 283 $OH \approx OH_{sh}^{eq}$ with good precision. The dependence of the boundary height, $z_{OH_{sh}^{eq}}$, on the season and
 284 latitude mainly repeats the behavior of $z_{HO_2_{sh}^{eq}}$. In particular $z_{OH_{sh}^{eq}}$ varies in the interval between 73 and 85
 285 km. At middle latitudes $z_{OH_{sh}^{eq}}$ in summer is several km higher than in winter. Near the equator $z_{OH_{sh}^{eq}}$ also
 286 demonstrates the weakest annual variations and varies in the range of 81-83 km. Nevertheless, in some
 287 cases the OH equilibrium boundary lies slightly higher than the HO₂ boundary. In particular it can be seen
 288 in April-August above 50°S, which can be explained by the difference between HO₂ and OH lifetimes
 289 ($\tau_{HO_2} < \tau_{OH}$), mainly due to $k_{18} > k_{17}$. Comparing with Figure 2, one can see the exclusion of the
 290 mentioned reactions from consideration results in the absence of the OH equilibrium areas at the low and
 291 middle mesosphere altitudes, as expected.

292

293 **6 The criteria for HO₂ and OH equilibrium validity in the upper mesosphere and lower** 294 **thermosphere**

295 Firstly we determine HO₂ and OH lifetimes and the local time scales of $HO_2_{sh}^{eq}$ and OH_{sh}^{eq} ,
 296 according to Section 2.

297 From Eqs. (2-3) and (9), HO₂ lifetime and the local time scales of $HO_2_{sh}^{eq}$ are as follows:

$$298 \tau_{HO_2} = \frac{1}{k_{18} \cdot O + (k_{14} + k_{15} + k_{16}) \cdot H}, \quad (11)$$

$$299 \tau_{HO_2_{sh}^{eq}} = \frac{HO_2_{sh}^{eq}}{|dHO_2_{sh}^{eq}/dt|}. \quad (12)$$

300 Then we find the expression for $dHO_2_{sh}^{eq}/dt$:

$$301 \frac{dHO_2_{sh}^{eq}}{dt} = \frac{k_{18} \cdot k_{20} \cdot M \cdot O_2 \cdot \frac{d}{dt} \left(\frac{H}{O} \right) \cdot O^2}{(k_{18} \cdot O + (k_{14} + k_{15} + k_{16}) \cdot H)^2} = - \frac{k_{18} \cdot k_{20} \cdot M \cdot O_2 \cdot \frac{d}{dt} \left(\frac{O}{H} \right) \cdot H^2}{(k_{18} \cdot O + (k_{14} + k_{15} + k_{16}) \cdot H)^2}. \quad (13)$$

302 Kulikov et al. (2023a) analyzed the local nighttime evolution of O and H within the framework of pure
 303 HO_x – O_x chemistry and found the expression for $\frac{d}{dt} \left(\frac{O}{H} \right)$:

$$304 \quad \frac{d}{dt} \left(\frac{O}{H} \right) = -2 \cdot k_{20} \cdot M \cdot O_2 \cdot \left(1 - \frac{k_{15} + k_{16}}{k_{18}} \right) - k_{21} \cdot O_3 - k_{12} \cdot M \cdot O_2 \cdot \frac{O}{H}. \quad (14)$$

305 Thus, Eq. (13) can be rewritten in the following form:

$$306 \quad \frac{dHO_{2sh}^{eq}}{dt} = \frac{k_{18} \cdot k_{20} \cdot M \cdot O_2 \cdot H^2 \cdot \left(2 \cdot k_{20} \cdot M \cdot O_2 \cdot \left(1 - \frac{k_{15} + k_{16}}{k_{18}} \right) + k_{21} \cdot O_3 + k_{12} \cdot M \cdot O_2 \cdot \frac{O}{H} \right)}{(k_{18} \cdot O + (k_{14} + k_{15} + k_{16}) \cdot H)^2}. \quad (15)$$

307 By combining Eqs. (9), (12), and (15) we obtain the expression for the local time scales of HO_{2sh}^{eq} :

$$308 \quad \tau_{HO_{2sh}^{eq}} = \frac{(k_{18} \cdot O + (k_{14} + k_{15} + k_{16}) \cdot H)}{k_{18} \cdot H \cdot \left(2 \cdot k_{20} \cdot M \cdot O_2 \cdot \left(1 - \frac{k_{15} + k_{16}}{k_{18}} \right) + k_{21} \cdot O_3 + k_{12} \cdot M \cdot O_2 \cdot \frac{O}{H} \right)}. \quad (16)$$

309 Thus, taking into account Eqs. (4), (11) and (16), the criterion for HO₂ equilibrium validity is written in
 310 the form:

$$311 \quad Crit_{HO_2} = \frac{\tau_{HO_2}}{\tau_{HO_{2sh}^{eq}}} = \frac{k_{18} \cdot H \cdot \left(2 \cdot k_{20} \cdot M \cdot O_2 \cdot \left(1 - \frac{k_{15} + k_{16}}{k_{18}} \right) + k_{21} \cdot O_3 + k_{12} \cdot M \cdot O_2 \cdot \frac{O}{H} \right)}{(k_{18} \cdot O + (k_{14} + k_{15} + k_{16}) \cdot H)^2} \leq 0.1. \quad (17)$$

312 We calculated $Crit_{HO_2}$, using the global 3D chemical transport model, and included the zonally and
 313 monthly averaged lines $\langle Crit_{HO_2} \rangle = 0.1$ in Figure 5 (see magenta lines). One can see that, depending
 314 on the month, each magenta line reproduces well the lower boundary of the main HO₂ equilibrium area
 315 and follows almost all its features and variations. Note, that in the zeroth order approximation the
 316 criterion (17) can be simplified as

$$317 \quad Crit_{HO_2} \approx \left(2 \cdot k_{20} \cdot M \cdot O_2 \cdot \left(1 - \frac{k_{15} + k_{16}}{k_{18}} \right) + k_{21} \cdot O_3 + k_{12} \cdot M \cdot O_2 \cdot \frac{O}{H} \right) \cdot \frac{H}{k_{18} \cdot O^2} \leq 0.1. \quad (18)$$

318 From Eqs. (2-3) and (10), OH lifetime and the local time scales of OH_{sh}^{eq} are as follows:

$$319 \quad \tau_{OH} = \frac{1}{k_{17} \cdot O}, \quad (19)$$

$$320 \quad \tau_{OH_{sh}^{eq}} = \frac{OH_{sh}^{eq}}{|dOH_{sh}^{eq}/dt|}. \quad (20)$$

321 Before determining the expression for dOH_{sh}^{eq}/dt one should keep in mind, that the expression (10)
 322 depends on the HO₂ concentration. As previously mentioned, near and above the OH equilibrium
 323 boundary HO₂ is in equilibrium ($HO_2 \approx HO_{2sh}^{eq}$) and we can use Eq. (9). In view of $k_{18} \cdot O \gg$
 324 $(k_{14} + k_{15} + k_{16}) \cdot H$,

$$325 \quad HO_{2sh}^{eq} \approx \frac{k_{20} \cdot H \cdot M \cdot O_2}{k_{18} \cdot O} \left(1 - \frac{(k_{14} + k_{15} + k_{16}) \cdot H}{k_{18} \cdot O} \right). \quad (21)$$

326 The substitution of Eq. (21) into Eq. (10) yields:

$$327 \quad OH_{sh}^{eq} = k_{20} \cdot H \cdot M \cdot O_2 \cdot \frac{(1 + \frac{2 \cdot k_{14} \cdot H}{k_{18} \cdot O}) \cdot (1 - \frac{(k_{14} + k_{15} + k_{16}) \cdot H}{k_{18} \cdot O})}{k_{17} \cdot O} + \frac{k_{21} \cdot H \cdot O_3}{k_{17} \cdot O} \approx \frac{k_{20} \cdot H \cdot M \cdot O_2}{k_{17} \cdot O} \cdot \left(1 + \frac{(k_{14} - k_{15} - k_{16}) \cdot H}{k_{18} \cdot O}\right) +$$

$$328 \quad \frac{k_{21} \cdot H \cdot O_3}{k_{17} \cdot O} \quad (22)$$

329 Thus, the expression for dOH_{sh}^{eq}/dt is:

$$330 \quad \frac{dOH_{sh}^{eq}}{dt} = \frac{d}{dt} \left(\frac{H}{O}\right) \cdot \left(\frac{k_{20} \cdot M \cdot O_2}{k_{17}} \cdot \left(1 + \frac{2 \cdot (k_{14} - k_{15} - k_{16}) \cdot H}{k_{18} \cdot O}\right) + \frac{k_{21} \cdot O_3}{k_{17}}\right) + \frac{k_{21} \cdot H}{k_{17} \cdot O} \frac{dO_3}{dt}. \quad (23)$$

331 Taking into account Eq. (14) and the differential equation for O_3 time evolution:

$$332 \quad \frac{dO_3}{dt} = k_{12} \cdot M \cdot O_2 \cdot O - k_{21} \cdot H \cdot O_3,$$

333 the expression (23) can be rewritten in following form:

$$334 \quad \frac{dOH_{sh}^{eq}}{dt} = \frac{(2 \cdot k_{20} \cdot M \cdot O_2 \cdot (1 - \frac{k_{15} + k_{16}}{k_{18}}) + k_{21} \cdot O_3 + k_{12} \cdot M \cdot O_2 \cdot \frac{O}{H}) \cdot H^2}{O^2} \cdot \left(\frac{k_{20} \cdot M \cdot O_2}{k_{17}} \cdot \left(1 + \frac{2 \cdot (k_{14} - k_{15} - k_{16}) \cdot H}{k_{18} \cdot O}\right) + \frac{k_{21} \cdot O_3}{k_{17}}\right) +$$

$$335 \quad \frac{k_{21} \cdot H \cdot (k_{12} \cdot M \cdot O_2 \cdot O - k_{21} \cdot H \cdot O_3)}{k_{17} \cdot O}. \quad (24)$$

336 Thus, by combining Eqs. (4), (19), (20), (22), and (24) we obtain the expression for the criterion for OH
337 equilibrium validity:

$$338 \quad Crit_{OH} = \frac{\tau_{OH}}{\tau_{OH_{sh}^{eq}}} =$$

$$339 \quad \frac{\left(\left(2 \cdot k_{20} \cdot M \cdot O_2 \cdot \left(1 - \frac{k_{15} + k_{16}}{k_{18}}\right) + k_{21} \cdot O_3 \cdot \frac{H}{O} + k_{12} \cdot M \cdot O_2\right) \cdot \left(k_{20} \cdot M \cdot O_2 \cdot \left(1 + \frac{2 \cdot (k_{14} - k_{15} - k_{16}) \cdot H}{k_{18} \cdot O}\right) + k_{21} \cdot O_3\right) + k_{21} \cdot (k_{12} \cdot M \cdot O_2 \cdot O - k_{21} \cdot H \cdot O_3)\right)}{k_{17} \cdot O \cdot \left(k_{20} \cdot M \cdot O_2 \cdot \left(1 + \frac{(k_{14} - k_{15} - k_{16}) \cdot H}{k_{18} \cdot O}\right) + k_{21} \cdot O_3\right)} \leq$$

$$340 \quad 0.1. \quad (25)$$

341 We calculated $Crit_{OH}$, using the global 3D chemical transport model, and included the zonally and
342 monthly averaged lines $\langle Crit_{OH} \rangle = 0.1$ in Figure 6 (see magenta lines). One can see that, depending on
343 the month, the magenta line almost everywhere reproduces the lower boundary of the OH equilibrium
344 area and repeats mainly its features and variations. Nevertheless, there are a few (by latitude) narrow
345 areas (in April-August near 70°S and in October-December near 70°N), where the criterion gives a few
346 km lower position of the OH equilibrium boundary, these are discussed in the next section. Note, that our
347 numerical analysis shows that in the zeroth order approximation the criterion (25) can be simplified as:

$$348 \quad Crit_{OH} \approx \left(2 \cdot k_{20} \cdot M \cdot O_2 \cdot \left(1 - \frac{k_{15} + k_{16}}{k_{18}}\right) + k_{21} \cdot O_3 + k_{12} \cdot M \cdot O_2 \cdot \frac{O}{H}\right) \cdot \frac{H}{k_{17} \cdot O^2} \leq 0.1. \quad (26)$$

349

350 7 Discussion

We now discuss obtained results and their possible applications.

Pay attention to the fact, that the presented results were plotted, using the lower threshold at 105° for the nighttime solar zenith angle (χ) to exclude the twilight transition processes. Nevertheless, our additional analysis revealed, that OH and HO₂ equilibrium conditions are fulfilled at $\chi > 95^\circ$. Evidently, during the processing of the measurement data, taking twilight χ in ($95^\circ, 105^\circ$) range into account extends the latitude range of OH and HO₂ equilibria application and allows us to include a noticeable part of the data into consideration. However, in this case one should check for additional condition (Kulikov et al., 2023a):

$$e^{\int_{lt_{bn}}^{lt} \tau_{HO_2}^{-1} dt} \gg 1, e^{\int_{lt_{bn}}^{lt} \tau_{OH}^{-1} dt} \gg 1, \quad (27)$$

where τ_{HO_2} and τ_{OH} are the HO₂ and OH lifetimes, determined by Eqs. (11) and (19), lt is local time of data, lt_{bn} is the local time at the beginning of the night. Mind, that at night O and H tend to decrease due to the shutdown of the O_x and HO_x family photochemical sources, so τ_{HO_2} and τ_{OH} increase. Thus, analyzing the measurement data one can apply more stringent conditions:

$$e^{\frac{lt-lt_{bn}}{\tau_{HO_2}}} \gg 1, e^{\frac{lt-lt_{bn}}{\tau_{OH}}} \gg 1. \quad (28)$$

The main results were obtained using a 3D model, where temperature and wind distributions are updated every 24 hours. This excluded the influence of the atmospheric wave motion, in particular, associated with tides, which is one of the main dynamical drivers in the tropical mesopause. We carried out additional modeling with the distributions of the main characteristics, calculated by the Canadian Middle Atmosphere Model for the year 2009 (Scinocca et al., 2008) with a 6-hourly frequency for updating. The analysis of the time-height evolution of OH and HO₂, especially at low latitudes, showed that our criteria reproduce quite well the local variations of the OH and HO₂ equilibrium boundaries in such conditions.

We evaluated the sensitivity of the presented HO₂ and OH criteria ($Crit_{HO_2}$ and $Crit_{OH}$) to the uncertainties of characteristics, involved in the expressions (17) and (25). The local heights of the OH and HO₂ equilibrium boundaries ($z_{HO_2}^{crit}$ and z_{OH}^{crit}) according to the criteria are determined as the altitudes, at which $Crit_{HO_2} = 0.1$ and $Crit_{OH} = 0.1$ respectively. We considered the whole dataset of nighttime profiles, obtained by the numerical simulation of a one-year global evolution of mesosphere – lower thermosphere, and estimated total uncertainties to determination of $z_{HO_2}^{crit}$ and z_{OH}^{crit} from each local (in time and space) dataset (profiles of O, H, O₃, M, O₂ and temperature). Following the typical analysis presented, for example in Mlynchak et al. (2013a, 2014), each uncertainty was calculated as a root sum square of the sensitivities to the individual perturbations of certain variables or parameters in the

382 expressions (17) and (25). The following uncertainties of the variables were used: 5K in the temperature
 383 and 30% in O_3 , O , and H . The uncertainties in reaction rates and their temperature dependencies were
 384 taken from Burkholder et al. (2020). As the result (see Figure 7), the monthly and longitudinally mean of
 385 total uncertainties in determination of $z_{HO_2}^{crit}$ and z_{OH}^{crit} were found varying in the range 0.02-1 km,
 386 depending on altitude and season. Note, that these values are comparable with the typical height
 387 resolution of satellite data. The latter allows us to consider our criteria as a robust instrument for
 388 equilibrium condition validation. The main reason of relatively low sensitivity of $z_{HO_2}^{crit}$ and z_{OH}^{crit} is
 389 the strong height-dependence of $Crit_{HO_2}$ and $Crit_{OH}$ near the value of 0.1.

390 As noted, Figs. 5-6 represent an interesting peculiarity. At the middle latitudes summer $z_{HO_2_{sh}}^{eq}$ and
 391 $z_{OH_{sh}}^{eq}$ are remarkably higher than winter ones. Recently, Kulikov et al. (2023b) found such a feature in
 392 the evolution of nighttime ozone chemical equilibrium boundary, derived from SABER/TIMED data,
 393 which was accompanied by the same variation of the transition zone, separating deep and weak
 394 photochemical oscillations of O and H , caused by the diurnal variations of solar radiation. The authors
 395 analyzed this effect near and below the transition zone. It was shown firstly, that nighttime O decreases
 396 with the characteristic time scale $\tau_o = O/|dO/dt|$ proportional to the O/H ratio at the beginning of the
 397 night. Secondly, during the summer the daytime O/H at the middle latitudes is remarkably less than the
 398 one in winter. Consequently, summer values of τ_o are significantly shorter than winter ones, so summer
 399 O during the night decreases much faster than in winter. In our case lifetimes of HO_2 and OH are
 400 proportional mainly to $\frac{1}{O}$ (see Eqs. (11) and (19)), so the summer rise of $z_{HO_2_{sh}}^{eq}$ and $z_{OH_{sh}}^{eq}$ can be
 401 explained by the season difference in O diurnal evolution at these latitudes.

402 As noted, there are a few narrow areas near 70°S/N (Figure 6), where the criterion (25) does not
 403 correspond well to the OH equilibrium boundary. Our analysis revealed, that the main reason is
 404 neglecting the reaction $OH+CO \rightarrow H+CO_2$ as the source of H in the corresponding differential equation
 405 of its chemical balance. In order to improve the criterion we revised the derivation of expression (14) for
 406 $\frac{d}{dt}\left(\frac{O}{H}\right)$ following to Kulikov et al. (2023a):

$$407 \frac{d}{dt}\left(\frac{O}{H}\right) = -2 \cdot k_{20} \cdot M \cdot O_2 \cdot \left(1 - \frac{k_{15}+k_{16}}{k_{18}}\right) - k_{21} \cdot O_3 - k_{12} \cdot M \cdot O_2 \cdot \frac{O}{H} - \frac{k_{32} \cdot CO}{k_{17} \cdot H} \cdot (k_{20} \cdot M \cdot O_2 \cdot (1 +$$

$$408 \frac{(k_{14}-k_{15}-k_{16}) \cdot H}{k_{18} \cdot O}) + k_{21} \cdot O_3)). \quad (29)$$

409 As a result the corrected criterion for OH equilibrium validity is as follows:

$$\begin{aligned}
410 \quad Crit_{OH}^m &= \frac{2 \cdot k_{20} \cdot M \cdot O_2 \cdot \left(1 - \frac{k_{15} + k_{16}}{k_{18}}\right) + k_{21} \cdot O_3 + k_{12} \cdot M \cdot O_2 \cdot \frac{O}{H} + \frac{k_{32} \cdot CO}{k_{17} \cdot H} \cdot (k_{20} \cdot M \cdot O_2 \cdot \left(1 + \frac{(k_{14} - k_{15} - k_{16}) \cdot H}{k_{18} \cdot O}\right) + k_{21} \cdot O_3)}{k_{17} \cdot O \cdot (k_{20} \cdot M \cdot O_2 \cdot \left(1 + \frac{(k_{14} - k_{15} - k_{16}) \cdot H}{k_{18} \cdot O}\right) + k_{21} \cdot O_3)} \cdot \frac{H}{O} \\
411 \quad &\left(k_{20} \cdot M \cdot O_2 \cdot \left(1 + \frac{2 \cdot (k_{14} - k_{15} - k_{16}) \cdot H}{k_{18} \cdot O}\right) + k_{21} \cdot O_3\right) + \frac{k_{21} \cdot (k_{12} \cdot M \cdot O_2 \cdot O - k_{21} \cdot H \cdot O_3)}{k_{17} \cdot O \cdot (k_{20} \cdot M \cdot O_2 \cdot \left(1 + \frac{(k_{14} - k_{15} - k_{16}) \cdot H}{k_{18} \cdot O}\right) + k_{21} \cdot O_3)} \leq 0.1 \quad (30)
\end{aligned}$$

412 We calculated this criterion, using the global 3D chemical transport model and included the zonally and
413 monthly averaged lines $\langle Crit_{OH}^m \rangle = 0.1$ on the OH equilibrium maps (see Figure 8). One can see that,
414 the inclusion of this additional term actually eliminates the noted discrepancy between OH boundary and
415 criterion. But the application of this criterion requires CO data.

416 As noted in the Introduction, the conditions of nighttime OH and HO₂ equilibria together with one
417 for O₃ equilibrium and their analytical criteria constitute a useful tool for retrieval of these components or
418 other characteristics (for example, O and H) from measured data. At the altitudes of upper mesosphere –
419 lower thermosphere these conditions can be applied, for example, to MLS/Aura database (measured
420 characteristics: OH, HO₂, O₃, and CO), SMILES (HO₂ and O₃), SCIAMACHY (O(¹S) green-line, O₂ A-
421 band, and OH Meinel band emissions), SABER/TIMED (O₃, OH Meinel band emissions at 2.0 μm (9→7
422 and 8→6 bands) and at 1.6 μm (5→3 and 4→2 bands)) and other, including improvement of existing
423 retrieval approaches. In particular, Panka et al. (2021) proposed the method of simultaneous derivation of
424 O and OH at the levels v=0-9 from SABER data (volume emission rates at 2.0 and 1.6 μm, $VER_{2\mu m}$ and
425 $VER_{1.6\mu m}$) at 80-100 km, taking into account the equilibrium condition for all states of OH. Such
426 approach is valid for excited states due to their very short lifetimes determined by radiative transitions
427 and quenching with O₂, N₂, and O. In the case of the OH ground state its lifetime is determined by the
428 reaction OH+O → H+O₂ only. It means, that Panka et al. (2021) used an equilibrium condition for total
429 OH, which, as one can see from Figure 6, may be significantly disrupted above 80 km. On the other hand,
430 there are latitude ranges and months, when the OH equilibrium boundary drops remarkably below 80 km.
431 Moreover, the Panka et al. method requires external data about HO₂, since the reaction HO₂+O → OH+O₂
432 becomes the important source for OH below 87 km (Panka et al., 2021; see also Figure 4 in our paper).

433 The results of our paper allow modifying the Panka et al. method to extend its capabilities. The
434 simplest development of this method seems to be the following. First of all, note that the HO₂ equilibrium
435 condition (9) depends on H and O only and can be used within the self-consistent retrieval procedure,
436 considering the following system of equations:

$$437 \quad OH(v = 1 - 9) = \frac{k_{12} \cdot H \cdot O_3 \cdot M \cdot f(v) + \sum_{v' > v} (a_1(v', v) + a_2(v', v) \cdot O_2 + a_3(v', v) \cdot N_2 + (a_4(v', v) + a_5(v', v)) \cdot O) \cdot OH(v')}{a_6(v) \cdot O + \sum_{v' > v} (a_1(v, v') + a_2(v, v') \cdot O_2 + a_3(v, v') \cdot N_2 + (a_4(v, v') + a_5(v, v')) \cdot O)},$$

$$438 \quad OH(0) = \frac{\sum_{v' > 0} (a_1(v', 0) + a_2(v', 0) \cdot O_2 + a_3(v', 0) \cdot N_2 + (a_4(v', 0) + a_5(v', 0)) \cdot O) \cdot OH(v') + k_{18} \cdot O \cdot HO_2 + 2 \cdot k_{14} \cdot H \cdot HO_2}{k_{17} \cdot O},$$

$$439 \quad HO_2 = \frac{k_{20} \cdot H \cdot M \cdot O_2}{k_{18} \cdot O + (k_{14} + k_{15} + k_{16}) \cdot H},$$

440 $VER_{2\mu m} = a_1(9,7) \cdot OH(9) + a_1(8,9) \cdot OH(8),$

441 $VER_{1.6\mu m} = a_1(5,3) \cdot OH(5) + a_1(4,2) \cdot OH(4),$

442 where a_{1-6} are the constant rates of the processes $OH(v) \rightarrow OH(v' < v) + hv$, $OH(v) + O_2 \rightarrow OH(v < v') +$
 443 O_2 , $OH(v) + N_2 \rightarrow OH(v < v') + N_2$, $OH(v) + O(^3P) \rightarrow OH(v' \leq v-5) + O(^1D)$, $OH(v) + O(^3P) \rightarrow OH(v' < v) +$
 444 $O(^3P)$, and $OH(v) + O(^3P) \rightarrow H + O_2$ respectively. Take into consideration, that this system includes 13
 445 equations with 13 unknown variables. Therefore, the solution to the system for a single set of the SABER
 446 measurements (simultaneously measured profiles of O_3 , T, pressure, $VER_{2\mu m}$, and $VER_{1.6\mu m}$) gives one
 447 simultaneously retrieved profiles of O, H, $OH(v=0-9)$, and HO_2 . By applying the criteria (17) and (25) to
 448 obtained O and H profiles, we verify the fulfillment of OH and HO_2 equilibrium conditions and determine
 449 the height, below which the resulting profiles should be cut. More advanced retrieval procedure would be
 450 statistical, based on Bayesian theorem, taking into account the uncertainties in measurement data and rate
 451 constants. Similarly, for example, to Kulikov et al. (2018a), it should include a derivation of posterior
 452 conditional probability density function of retrieved characteristics and numerical analysis of this
 453 function. Detailed development of this retrieval method is outside of this paper and should be carried out
 454 in a separate work.

455

456

457 **8 Conclusions**

458 The presented analysis shows, that there are extended areas in mesosphere and lower thermosphere,
 459 where nighttime HO_2 and OH are close to their local equilibrium concentrations, determined mainly by
 460 the reactions between $HO_x - O_x$ components among themselves and with H_2O_2 , N, NO, NO_2 , and CO. In
 461 upper mesosphere – lower thermosphere the shortened expressions for their local equilibrium
 462 concentrations are valid, including the $HO_x - O_x$ chemistry only. These conditions describe the HO_2 and
 463 OH equilibrium from the top to some lower boundaries, the altitude position of which vary in the interval
 464 between 73 and 85 km and depends essentially on the season and latitude. We proposed analytical
 465 criteria, which almost everywhere reproduces quite well the main features of these boundaries. Due to
 466 weak sensitivity to uncertainties of reaction rates and variables, these criteria can be considered a robust
 467 instrument for HO_2 and OH equilibrium validation. The obtained results allow extending the abilities of
 468 the Panka et al. (2021) method to retrieve unmeasured components from SABER data. The simultaneous
 469 application of OH and HO_2 equilibrium conditions to the SABER data together with the OH and HO_2
 470 criteria to control this equilibrium validity allows us to retrieve all unknown $HO_x - O_x$ components (O, H,
 471 OH, and HO_2) and to extend the altitude range of retrieval downward below 80 km and without external
 472 information.

473

474 **Data availability.** CMAM data are obtained from the website ([https://climate-](https://climate-modelling.canada.ca/climatemodeldata/cmam/cmam30/)
475 [modelling.canada.ca/climatemodeldata/cmam/cmam30/](https://climate-modelling.canada.ca/climatemodeldata/cmam/cmam30/), last access: 18 May 2024).

476

477 **Code availability.** Code is available upon request.

478

479 **Author contributions.** Conceptualization: MK, MB, AC, SD, AF. Methodology: MK, AF.
480 Investigation: MK, MB, AC, SD. Software: MB, AC. Visualization: MB, AC. Funding Acquisition: MK.
481 Writing – original draft preparation: MK, MB. Writing – review & editing: AC, SD. Supervising: AF.

482

483 **Competing interests.** The authors declare no conflict of interest.

484

485 **Acknowledgements.** The paper is in the memory of Prof. G.M. Fraiman. The authors are grateful to
486 reviewers for providing valuable recommendations to improve the paper.

487

488 **Financial support.** The main results presented in Sects. 3-6 were obtained with the support of the
489 Russian Science Foundation under grant No. 22-12-00064 (<https://rscf.ru/project/22-12-00064/>, last
490 access: 18 May 2024). The analysis in Discussion was carried out at the expense of state assignment No.
491 0729-2020-0037.

492

493 **Supplement link:**

494

495 **References**

496 Avallone, L. M. and Toohey, D. W.: Tests of halogen photochemistry using in situ measurements of ClO
497 and BrO in the lower polar stratosphere, *J. Geophys. Res.*, 106, 10411–1042,
498 <https://doi.org/10.1029/2000JD900831>, 2001.

499 Belikov, M. V., Kulikov, M. Yu, Grygalashvyly, M., Sonnemann, G. R., Ermakova, T. S., Nechaev,
500 A. A., and Feigin, A. M.: Ozone chemical equilibrium in the extended mesopause under the nighttime
501 conditions, *Adv. Space Res.*, 61, 426–432, <https://doi.org/10.1016/j.asr.2017.10.010>, 2018.

502 Berger, U., and U. von Zahn (1999), Two level structure of the mesopause: A model study, *J. Geophys.*
503 *Res.*, 104, 22,083–22,093.

504 Burkholder, J. B., Sander, S. P., Abbatt, J., Barker, J. R., Cappa, C., Crouse, J. D., Dibble, T. S., Huie,
505 R. E., Kolb, C. E., Kurylo, M. J., Orkin, V. L., Percival, C. J., Wilmouth, D. M., and Wine, P. H.:
506 Chemical Kinetics and Photochemical Data for Use in Atmospheric Studies, Evaluation No. 19, JPL
507 Publication 19-5, Jet Propulsion Laboratory, Pasadena, <http://jpldataeval.jpl.nasa.gov>, 2020.

508 Cantrell, C. A., Mauldin, L., Zondlo, M., Eisele, F., Kosciuch, E., Shetter, R., Lefer, B., Hall, S., Campos,
509 T., Ridley, B., Walega, J., Fried, A., Wert, B., Flocke, F., Weinheimer, A., Hannigan, J., Coffey, M.,
510 Atlas, E., Stephens, S., Heikes, B., Snow, J., Blake, D., Blake, N., Katzenstein, A., Lopez, J., Browell, E.
511 V., Dibb, J., Scheuer, E., Seid, G., and Talbot, R.: Steady state free radical budgets and ozone
512 photochemistry during TOPSE, *J. Geophys. Res.*, 108, TOP9-1–TOP9-22,
513 <https://doi.org/10.1029/2002JD002198>, 2003.

514 Evans, W. F. J., and Llewellyn, E. J.: Atomic hydrogen concentrations in the mesosphere and the
515 hydroxyl emissions, *J. Geophys. Res.*, 78, 323–326, <https://doi.org/10.1029/JA078i001p00323>, 1973.

516 Evans, W. F. J., McDade, I. C., Yuen, J., and Llewellyn, E. J.: A rocket measurement of the O₂ infrared
517 atmospheric (0-0) band emission in the dayglow and a determination of the mesospheric ozone and
518 atomic oxygen densities, *Can. J. Phys.*, 66, 941–946, <https://doi.org/10.1139/p88-151>. 1988.

519 Fytterer, T., von Savigny, C., Mlynczak, M., and Sinnhuber, M.: Model results of OH airglow
520 considering four different wavelength regions to derive night-time atomic oxygen and atomic hydrogen in
521 the mesopause region, *Atmos. Chem. Phys.*, 19, 1835–1851, <https://doi.org/10.5194/acp-19-1835-2019>,
522 2019.

523 Good, R. E.: Determination of atomic oxygen density from rocket borne measurements of hydroxyl
524 airglow, *Planet. Space Sci.*, 24, 389–395, [https://doi.org/10.1016/0032-0633\(76\)90052-0](https://doi.org/10.1016/0032-0633(76)90052-0), 1976.

525 Grygalashvyly, M., Sonnemann, G. R., and Hartogh, P.: Long-term behavior of the concentration of the
526 minor constituents in the mesosphere - a model study, *Atmos. Chem. Phys.*, 9, 2779–2792,
527 <https://doi.org/10.5194/acp-9-2779-2009>, 2009.

528 Grygalashvyly, M., Sonnemann, G. R., Lübken, F.-J., Hartogh, P., and Berger, U.: Hydroxyl layer: Mean
529 state and trends at midlatitudes, *J. Geophys. Res. Atmos.*, 119, 12,391–12,419,
530 <https://doi.org/10.1002/2014JD022094>, 2014.

531 Grygalashvyly, M.: Several notes on the OH* layer, *Ann. Geophys.*, 33, 923-930,
532 <https://doi.org/10.5194/angeo-33-923-2015>, 2015.

533 Hartogh, P., Jarchow, C., Sonnemann, G. R., and Grygalashvyly, M.: On the spatiotemporal behavior of
534 ozone within the upper mesosphere/mesopause region under nearly polar night conditions, *J. Geophys.*
535 *Res.*, 109, D18303, <https://doi.org/10.1029/2004JD004576>, 2004.

536 Hartogh, P., Jarchow, Ch., Sonnemann, G. R., and Grygalashvyly, M.: Ozone distribution in the middle
537 latitude mesosphere as derived from microwave measurements at Lindau (51.66°N, 10.13°E), *J. Geophys.*
538 *Res.*, 116, D04305, <https://doi.org/10.1029/2010JD014393>, 2011.

539 Körner, U., and Sonnemann, G. R.: Global 3D-modeling of water vapor concentration of the
540 mesosphere/mesopause region and implications with respect to the NLC region, *J. Geophys. Res.*, 106,
541 9639–9651, <https://doi.org/10.1029/2000JD900744>, 2001.

542 Kowalewski, S., v. Savigny, C., Palm, M., McDade, I. C., and Notholt, J.: On the impact of the temporal
543 variability of the collisional quenching process on the mesospheric OH emission layer: a study based on
544 SD-WACCM4 and SABER, *Atmos. Chem. Phys.*, 14, 10193-10210, [https://doi.org/10.5194/acp-14-](https://doi.org/10.5194/acp-14-10193-2014)
545 10193-2014, 2014.

546 Kremp, C., Berger, U., Hoffmann, P., Keuer, D., and Sonnemann, G. R.: Seasonal variation of middle
547 latitude wind fields of the mesopause region—A comparison between observation and model calculation,
548 *Geophys. Res. Lett.*, 26, 1279–1282, <https://doi.org/10.1029/1999GL900218>, 1999.

549 Kulikov, M. Y., Feigin, A. M., and Sonnemann, G. R.: Retrieval of the vertical distribution of chemical
550 components in the mesosphere from simultaneous measurements of ozone and hydroxyl distributions,
551 *Radiophys. Quantum Electron.*, 49, 683–691, <https://doi.org/10.1007/s11141-006-0103-4>, 2006.

552 Kulikov, M. Yu., Feigin, A. M., and Sonnemann, G. R.: Retrieval of water vapor profile in the
553 mesosphere from satellite ozone and hydroxyl measurements by the basic dynamic model of mesospheric
554 photochemical system, *Atmos. Chem. Phys.*, 9, 8199–8210, <https://doi.org/10.5194/acp-9-8199-2009>,
555 2009.

556 Kulikov, M. Y., Belikovich, M. V., Grygalashvyly, M., Sonnemann, G. R., Ermakova, T. S., Nechaev, A.
557 A., and Feigin, A. M.: Daytime ozone loss term in the mesopause region, *Ann. Geophys.*, 35, 677-682
558 <https://doi.org/10.5194/angeo-35-677-2017>, 2017.

559 Kulikov, M. Y., Nechaev, A. A., Belikovich, M. V., Ermakova, T. S., and Feigin, A. M.: Technical note:
560 Evaluation of the simultaneous measurements of mesospheric OH, HO₂, and O₃ under a photochemical
561 equilibrium assumption – a statistical approach, *Atm. Chem. Phys.*, 18, 7453-747,
562 <https://doi.org/10.5194/acp-18-7453-2018>, 2018a.

563 Kulikov, M. Y., Belikovich, M. V., Grygalashvyly, M., Sonnemann, G. R., Ermakova, T. S., Nechaev, A.
564 A., and Feigin, A. M.: Nighttime ozone chemical equilibrium in the mesopause region. *J. Geophys.*
565 *Res.*, 123, 3228–3242, <https://doi.org/10.1002/2017JD026717>, 2018b.

566 Kulikov, M. Yu., Nechaev, A. A., Belikovich, M. V., Vorobeva, E. V., Grygalashvyly, M., Sonnemann,
567 G. R., and Feigin, A. M.: Border of nighttime ozone chemical equilibrium in the mesopause region from
568 SABER data: implications for derivation of atomic oxygen and atomic hydrogen, *Geophys. Res. Lett.*, 46,
569 997–1004, <https://doi.org/10.1029/2018GL080364>, 2019.

570 Kulikov, M. Y., Belikovich, M. V., Feigin, A. M.: The 2-day photochemical oscillations in the mesopause
571 region: the first experimental evidence? *Geophys. Res. Lett.*, 48, e2021GL092795,
572 <https://doi.org/10.1029/2021GL092795>, 2021.

573 Kulikov M.Yu., Belikovich, M.V., Grygalashvyly, M., Sonnemann, G. R., and Feigin, A.M.: Retrieving
574 daytime distributions of O, H, OH, HO₂, and chemical heating rate in the mesopause region from satellite
575 observations of ozone and OH* volume emission: The evaluation of the importance of the reaction
576 $H+O_3\rightarrow O_2+OH$ in the ozone balance, *Adv. Space Res.*, 69(9), 3362-3373,
577 <https://doi.org/10.1016/j.asr.2022.02.011>, 2022a.

578 Kulikov, M. Y., Belikovich, M. V., Grygalashvyly, M., Sonnemann, G. R., and Feigin, A.M.: The revised
579 method for retrieving daytime distributions of atomic oxygen and odd-hydrogens in the mesopause region
580 from satellite observations, *Earth, Planets and Space*, 74, 44, [https://doi.org/10.1186/s40623-022-01603-](https://doi.org/10.1186/s40623-022-01603-8)
581 8, 2022b.

582 Kulikov, M. Yu., Belikovich, M. V., Chubarov, A. G., Dementeyva, S. O., Feigin, A. M.: Boundary of
583 nighttime ozone chemical equilibrium in the mesopause region: improved criterion of determining the
584 boundary from satellite data, *Adv. Space Res.*, 71 (6), 2770-2780,
585 <https://doi.org/10.1016/j.asr.2022.11.005>, 2023a.

586 Kulikov, M. Yu., Belikovich, M. V., Chubarov, A. G., Dementyeva, S. O., and Feigin, A. M.: Boundary
587 of nighttime ozone chemical equilibrium in the mesopause region: long-term evolution determined using
588 20-year satellite observations, *Atmos. Chem. Phys.*, 23, 14593–14608, [https://doi.org/10.5194/acp-23-](https://doi.org/10.5194/acp-23-14593-2023)
589 14593-2023, 2023b.

590 Llewellyn, E. J., McDade, I. C. Moorhouse, P. and Lockertie M. D.: Possible reference models for
591 atomic oxygen in the terrestrial atmosphere, *Adv. Space Res.*, 13, 135–144, [https://doi.org/10.1016/0273-](https://doi.org/10.1016/0273-1177(93)90013-2)
592 1177(93)90013-2, 1993.

593 Llewellyn, E. J., and McDade, I. C.: A reference model for atomic oxygen in the terrestrial atmosphere,
594 *Adv. Space Res.*, 18, 209–226, [https://doi.org/10.1016/0273-1177\(96\)00059-2](https://doi.org/10.1016/0273-1177(96)00059-2), 1996.

595 Manney, G. L., Kruger, K., Sabutis, J. L., Sena, S. A., and Pawson, S.: The remarkable 2003–2004 winter
596 and other recent warm winters in the Arctic stratosphere since the late 1990s. *J. Geophys. Res.*, 110,
597 D04107, <https://doi.org/10.1029/2004JD005367>, 2005.

598 Marchand, M., Bekki, S., Lefevre, F., and Hauchecorne, A.: Temperature retrieval from stratospheric O₃
599 and NO₃ GOMOS data, *Geophys. Res. Lett.*, 34, L24809, <https://doi.org/10.1029/2007GL030280>, 2007.

600 Marsh, D. R., Smith, A. K., Mlynczak, M. G., and Russell III, J. M.: SABER observations of the OH
601 Meinel airglow variability near the mesopause, *J. Geophys. Res.*, 111, A10S05,
602 <https://doi.org/10.1029/2005JA011451>, 2006.

603 McDade, I. C., Llewellyn, E. J., and Harris, F. R.: Atomic oxygen concentrations in the lower auroral
604 thermosphere, *Adv. Space Res.*, 5, 229–232, <https://doi.org/10.1029/GL011I003P00247>, 1985.

605 McDade, I. C., and Llewellyn, E. J.: Mesospheric oxygen atom densities inferred from night-time OH
606 Meinel band emission rates, *Planet. Space Sci.*, 36, 897–905, [https://doi.org/10.1016/0032-](https://doi.org/10.1016/0032-0633(88)90097-9)
607 0633(88)90097-9, 1988.

608 Mlynczak, M. G., Marshall, B. T., Martin-Torres, F. J., Russell III, J. M., Thompson, R. E., Remsberg, E.
609 E., and Gordley, L. L.: Sounding of the Atmosphere using Broadband Emission Radiometry observations
610 of daytime mesospheric O₂(¹D) 1.27 μm emission and derivation of ozone, atomic oxygen, and solar and
611 chemical energy deposition rates, *J. Geophys. Res.*, 112, D15306, <https://doi.org/10.1029/2006JD008355>,
612 2007.

613 Mlynczak, M. G., Hunt, L. A., Mast, J. C., Marshall, B. T., Russell III, J. M., Smith, A. K., Siskind, D. E.,
614 Yee, J.-H., Mertens, C. J., Martin-Torres, F. J., Thompson, R. E., Drob, D. P., and Gordley, L. L.: Atomic
615 oxygen in the mesosphere and lower thermosphere derived from SABER: Algorithm theoretical basis and
616 measurement uncertainty, *J. Geophys. Res.*, 118, 5724–5735, <https://doi.org/10.1002/jgrd.50401>, 2013a.

617 Mlynczak, M. G., Hunt, L. H., Mertens, C. J., Marshall, B. T., Russell III, J. M., López-Puertas, M.,
618 Smith, A. K., Siskind, D. E., Mast, J. C., Thompson, R. E., and Gordley, L. L.: Radiative and energetic
619 constraints on the global annual mean atomic oxygen concentration in the mesopause region, *J. Geophys.*
620 *Res. Atmos.*, 118, 5796–5802, <https://doi.org/10.1002/jgrd.50400>, 2013b.

621 Mlynczak, M. G., Hunt, L. A. Marshall, B. T. Mertens, C. J. Marsh, D. R. Smith, A. K. Russell, J. M.
622 Siskind D. E., and Gordley L. L.: Atomic hydrogen in the mesopause region derived from SABER:
623 Algorithm theoretical basis, measurement uncertainty, and results, *J. Geophys. Res.*, 119, 3516–3526,
624 <https://doi.org/10.1002/2013JD021263>, 2014.

625 Mlynczak, M. G., Hunt, L. A., Russell, J. M. III, and Marshall, B. T.: Updated SABER night atomic
626 oxygen and implications for SABER ozone and atomic hydrogen, *Geophys. Res. Lett.*, 45, 5735–5741,
627 <https://doi.org/10.1029/2018GL077377>, 2018.

628 Morton, K. W., and Mayers, D. F.; *Numerical Solution of Partial Differential Equations*, Cambridge
629 University Press, 1994.

630 Nikoukar, R., Swenson, G. R., Liu, A. Z., and Kamalabadi, F.: On the variability of mesospheric OH
631 emission profiles, *J. Geophys. Res.*, 112, D19109, <https://doi.org/10.1029/2007JD008601>, 2007.

632 Panka, P. A., Kutepov, A. A., Zhu, Y., Kaufmann, M., Kalogerakis, K. S., Rezac, L., et al.: Simultaneous
633 retrievals of nighttime O(³P) and total OH densities from satellite observations of Meinel band emissions.
634 *Geoph. Res.Lett.*, 48, e2020GL091053, <https://doi.org/10.1029/2020GL091053>, 2021.

635 Pendleton, W. R., Baker, K. D., Howlett, L. C.: Rocket-based investigations of O(³P), O₂ (a¹Δ_g) and OH*
636 (v=1,2) during the solar eclipse of 26 February 1979, *J. Atm. Terr. Phys.*, 45(7), 479-491, 1983.

637 Siskind, D. E., Marsh, D. R., Mlynczak, M. G., Martin-Torres, F. J., and Russell III, J. M.: Decreases in
638 atomic hydrogen over the summer pole: Evidence for dehydration from polar mesospheric clouds?
639 *Geophys. Res. Lett.*, 35, L13809, <https://doi.org/10.1029/2008GL033742>, 2008.

640 Russell, J. P., and Lowe, R. P.: Atomic oxygen profiles (80-94 km) derived from Wind Imaging
641 Interferometer/Upper Atmospheric Research Satellite measurements of the hydroxyl airglow: 1.
642 Validation of technique, *J. Geophys. Res.*, 108(D21), 4662, <https://doi.org/10.1029/2003JD003454>, 2003.

643 Russell, J. P., Ward, W. E., Lowe, R. P., Roble, R. G., Shepherd, G. G., and Solheim, B.: Atomic oxygen
644 profiles (80 to 115 km) derived from Wind Imaging Interferometer/Upper Atmospheric Research Satellite
645 measurements of the hydroxyl and green line airglow: Local time–latitude dependence, *J. Geophys. Res.*,
646 110(D15), D15305, <https://doi.org/10.1029/2004JD005570>, 2005.

647 Siskind, D. E., Mlynczak, M. G., Marshall, T., Friedrich, M., Gumbel, J.: Implications of odd oxygen
648 observations by the TIMED/SABER instrument for lower D region ionospheric modeling, *J. Atmos. Sol.*
649 *Terr. Phys.*, 124, 63–70, <https://doi.org/10.1016/j.jastp.2015.01.014>, 2015.

650 Smith, A. K., Lopez-Puertas, M., Garcia-Comas, M. and Tukiainen, S.: SABER observations of
651 mesospheric ozone during NH late winter 2002–2009, *Geophys. Res. Lett.*, 36, L23804,
652 <https://doi.org/10.1029/2009GL040942>, 2009.

653 Smith, A. K., Marsh, D. R. Mlynczak, M. G. and Mast, J. C.: Temporal variations of atomic oxygen in the
654 upper mesosphere from SABER, *J. Geophys. Res.*, 115, D18309, <https://doi.org/10.1029/2009JD013434>,
655 2010.

656 Scinocca, J. F., McFarlane, N. A., Lazare, M., Li, J., and Plummer, D.: The CCCma third generation
657 AGCM and its extension into the middle atmosphere, *Atmos. Chem. Phys.*, 8, 7055–7074,
658 <https://doi.org/10.5194/acp-8-7055-2008>, 2008.

659 Sonnemann, G., Kremp, C. Ebel, A. and Berger U.: A three-dimensional dynamic model of minor
660 constituents of the mesosphere, *Atmos. Environ.*, 32, 3157–3172, [https://doi.org/10.1016/S1352-2310\(98\)00113-7](https://doi.org/10.1016/S1352-2310(98)00113-7), 1998.

662 Sonnemann, G. R., Grygalashvily, M., Hartogh, P., and Jarchow, C.: Behavior of mesospheric ozone
663 under nearly polar night conditions, *Adv. Space Res.*, 38, 2402–2407,
664 <https://doi.org/10.1016/j.asr.2006.09.011>, 2006.

665 Sonnemann, G. R., Hartogh, P., Grygalashvily, M., Li, S., and Berger, U.: The quasi 5-day signal in the
666 mesospheric water vapor concentration at high latitudes in 2003-a comparison between observations at
667 ALOMAR and calculations, *J. Geophys. Res.*, 113, D04101, <https://doi.org/10.1029/2007JD008875>,
668 2008.

669 Sonnemann, G. R., Hartogh, P., Berger, U., and Grygalashvily, M.: Hydroxyl layer: trend of number
670 density and intra-annual variability, *Ann. Geophys.*, 33, 749–767, [https://doi.org/10.5194/angeo-33-749-](https://doi.org/10.5194/angeo-33-749-2015)
671 2015, 2015.

672 Stedman, D. H., Chameides, W., and Jackson, J. O.: Comparison of experimental and computed values
673 for J(NO₂), *Geophys. Res. Lett.*, 2, 22–25, <https://doi.org/10.1029/GL002i001p00022>, 1975.

674 Swenson, G. R., and Gardner C. S.: Analytical models for the responses of the mesospheric OH* and Na
675 layers to atmospheric gravity waves, *J. Geophys. Res.*, 103(D6), 6271–6294,
676 <https://doi.org/10.1029/97JD02985>, 1998.

677 Thomas, R. J.: Atomic hydrogen and atomic oxygen density in the mesosphere region: Global and
678 seasonal variations deduced from Solar Mesosphere Explorer near-infrared emissions, *J. Geophys. Res.*,
679 95, 16,457–16,476, <https://doi.org/10.1029/JD095iD10p16457>, 1990.

680 Walcek, C. J.: Minor flux adjustment near mixing ratio extremes for simplified yet highly accurate
681 monotonic calculation of tracer advection, *J. Geophys. Res.*, 105, 9335-9348,
682 <https://doi.org/10.1029/1999JD901142>, 2000.

683 Xu, J., Smith, A. K., Jiang, G., Gao, H., Wei, Y., Mlynchzak, M. G., and Russell III, J. M.: Strong
684 longitudinal variations in the OH nightglow, *Geophys. Res. Lett.*, 37, L21801,
685 <https://doi.org/10.1029/2010GL043972>, 2010.

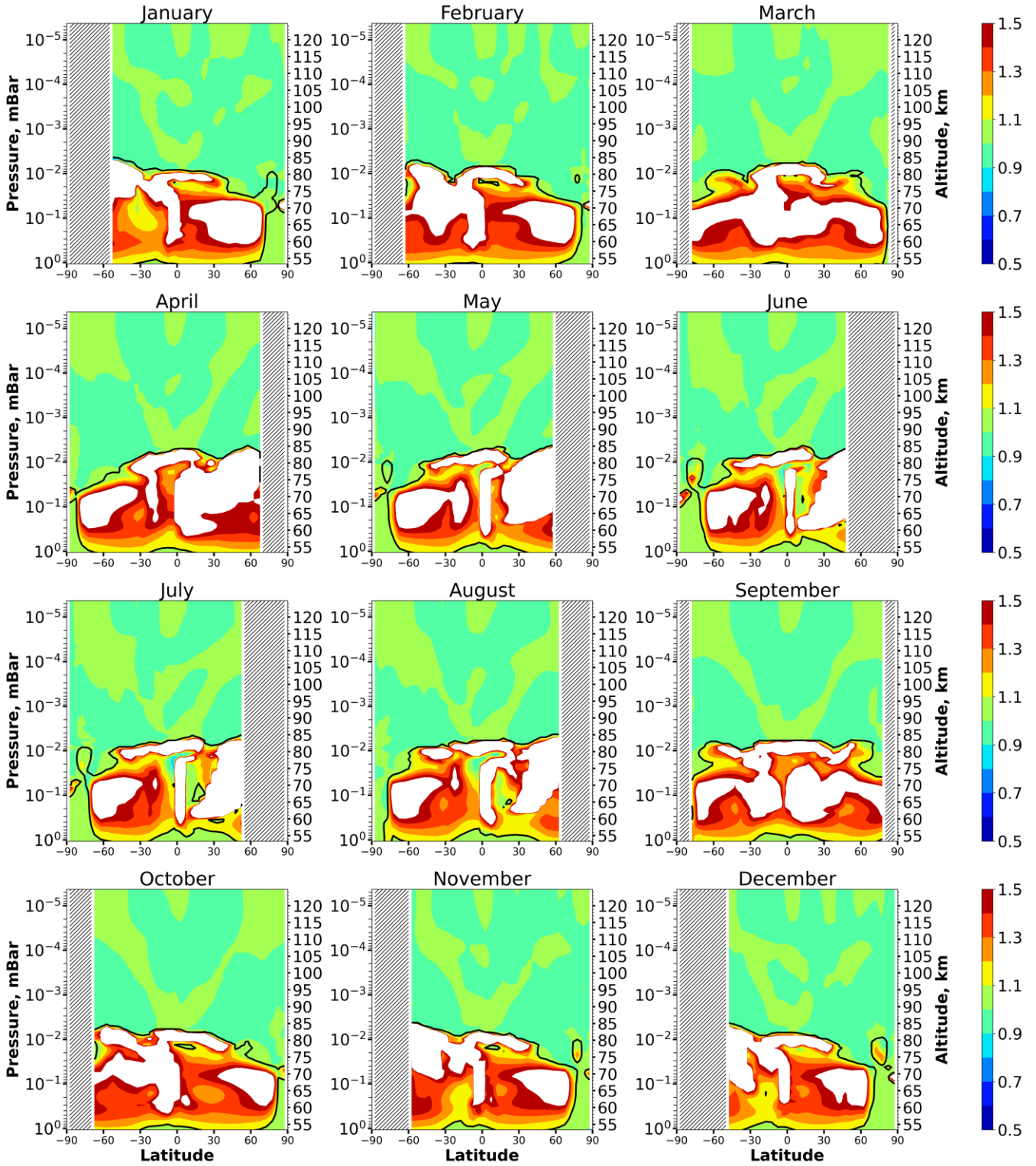
686 Xu, J., Gao, H. Smith, A. K. and Zhu Y.: Using TIMED/SABER nightglow observations to investigate
687 hydroxyl emission mechanisms in the mesopause region, *J. Geophys. Res.*, 117, D02301,
688 <https://doi.org/10.1029/2011JD016342>, 2012.

689 **Table 1.** List of reactions included in 3-d chemical transport model with the corresponding reaction rates
 690 taken from Burkholder et al. (2020).

1	$O(^1D)+O_2 \rightarrow O+O_2$	24	$H+OH+N_2 \rightarrow H_2O+N_2$	47	$NO+O_3 \rightarrow NO_2+O_2$
2	$O(^1D)+N_2 \rightarrow O+N_2$	25	$OH+H_2 \rightarrow H_2O+H$	48	$NO_2+O_3 \rightarrow NO_3+O_2$
3	$O(^1D)+O_3 \rightarrow O_2+2O$	26	$OH+OH \rightarrow H_2O+O$	49	$N+OH \rightarrow NO+H$
4	$O(^1D)+O_3 \rightarrow 2O_2$	27	$OH+OH+M \rightarrow H_2O_2+M$	50	$NO+HO_2 \rightarrow NO_2+OH$
5	$O(^1D)+N_2O \rightarrow 2NO$	28	$OH+HO_2 \rightarrow H_2O+O_2$	51	$H+NO_2 \rightarrow OH+NO$
6	$O(^1D)+N_2O \rightarrow N_2+O_2$	29	$H_2O_2+OH \rightarrow H_2O+HO_2$	52	$NO_3+NO \rightarrow 2NO_2$
7	$O(^1D)+H_2O \rightarrow 2OH$	30	$HO_2+HO_2 \rightarrow H_2O_2+O_2$	53	$N+NO \rightarrow N_2+O$
8	$O(^1D)+H_2 \rightarrow H+OH$	31	$HO_2+HO_2+M \rightarrow H_2O_2+O_2+M$	54	$N+NO_2 \rightarrow N_2O+O$
9	$O(^1D)+CH_4 \rightarrow CH_3+OH$	32	$OH+CO \rightarrow H+CO_2$	55	$O_2+h\nu \rightarrow 2O$
10	$O(^1D)+CH_4 \rightarrow H_2+CH_2O$	33	$CH_4+OH \rightarrow CH_3+H_2O$	56	$O_2+h\nu \rightarrow O+O(^1D)$
11	$O+O+M \rightarrow O_2+M$	34	$CH_3+O_2 \rightarrow CH_3O_2$	57	$O_3+h\nu \rightarrow O_2+O$
12	$O+O_2+M \rightarrow O_3+M$	35	$CH_3+O \rightarrow CH_2O+H$	58	$O_3+h\nu \rightarrow O_2+O(^1D)$
13	$O+O_3 \rightarrow O_2+O_2$	36	$CH_3O_2+NO \rightarrow CH_3O+NO_2$	59	$N_2+h\nu \rightarrow 2N$
14	$H+HO_2 \rightarrow 2OH$	37	$CH_3O+O_2 \rightarrow CH_2O+HO_2$	60	$NO+h\nu \rightarrow N+O$
15	$H+HO_2 \rightarrow H_2O+O$	38	$CH_2O \rightarrow H_2+CO$	61	$NO_2+h\nu \rightarrow NO+O$
16	$H+HO_2 \rightarrow H_2+O_2$	39	$CH_2O \rightarrow H+CHO$	62	$N_2O+h\nu \rightarrow N_2+O(^1D)$
17	$OH+O \rightarrow H+O_2$	40	$CHO+O_2 \rightarrow HO_2+CO$	63	$N_2O+h\nu \rightarrow N+NO$
18	$HO_2+O \rightarrow OH+O_2$	41	$O_3+N \rightarrow NO+O_2$	64	$NO_3+h\nu \rightarrow NO_2+O$
19	$H_2O_2+O \rightarrow OH+HO_2$	42	$NO_3+O \rightarrow NO_2+O_2$	65	$H_2O+h\nu \rightarrow H+OH$
20	$H+O_2+M \rightarrow HO_2+M$	43	$O+NO+M \rightarrow NO_2+M$	66	$H_2O_2+h\nu \rightarrow 2OH$
21	$H+O_3 \rightarrow OH+O_2$	44	$NO_2+O \rightarrow NO+O_2$	67	$CH_4+h\nu \rightarrow CH_2+H_2$
22	$OH+O_3 \rightarrow O_2+HO_2$	45	$NO_2+O+M \rightarrow NO_3+M$	68	$CH_4+h\nu \rightarrow CH+H_2+H$
23	$HO_2+O_3 \rightarrow OH+2O_2$	46	$N+O_2 \rightarrow NO+O$	69	$CO_2+h\nu \rightarrow CO+O$

691

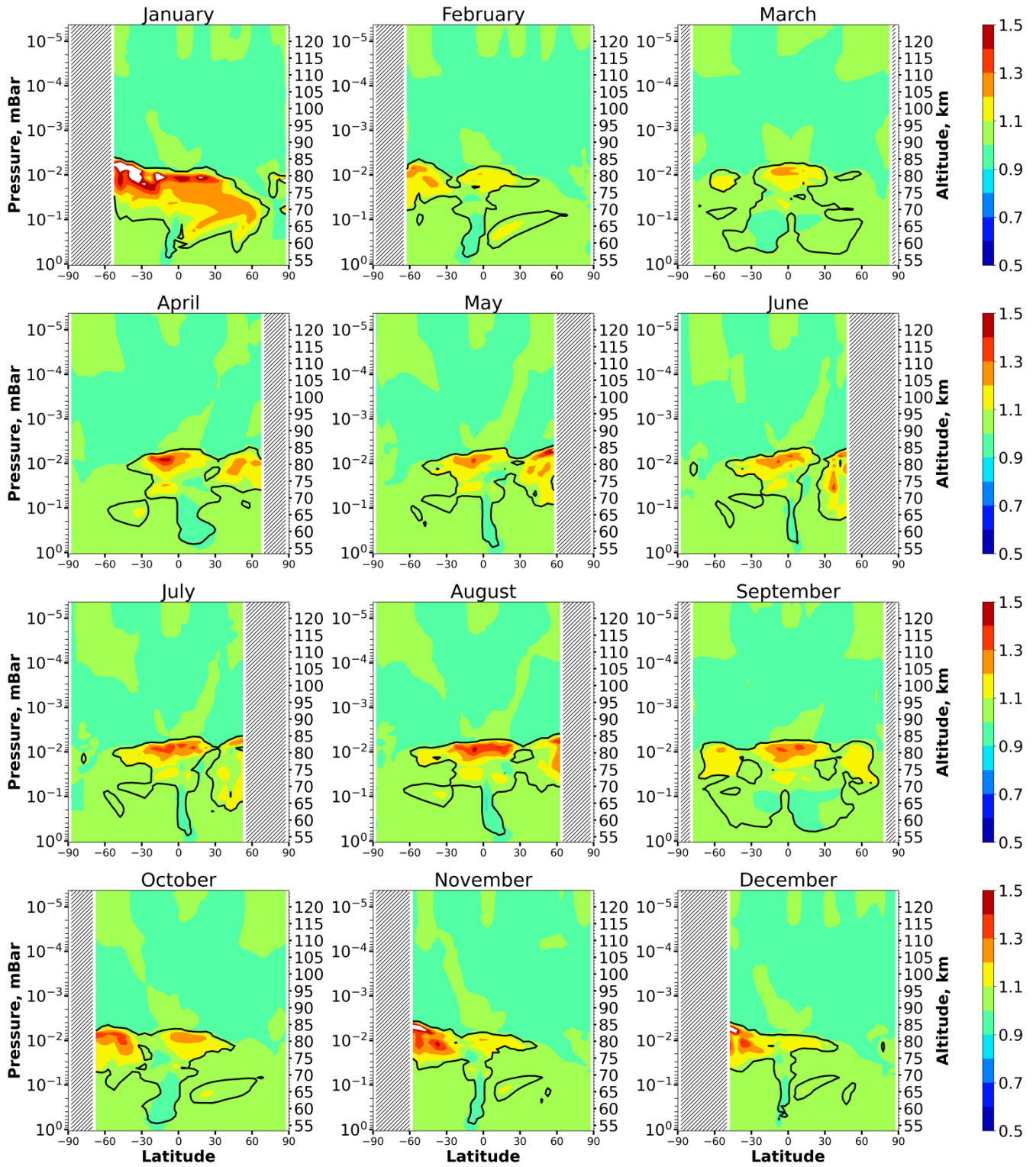
692



693

694 Figure 1. Nighttime mean and monthly averaged HO_2/HO_2^{eq} , where HO_2^{eq} is equilibrium concentration
 695 determined by Eq. (5). Black line shows the boundary of HO_2 equilibrium according to condition (1). The
 696 stippling corresponds to $\chi < 105^\circ$. The white area represents the $\langle HO_2/HO_2^{eq} \rangle$ ratio outside the [0.5,
 697 1.5] interval.

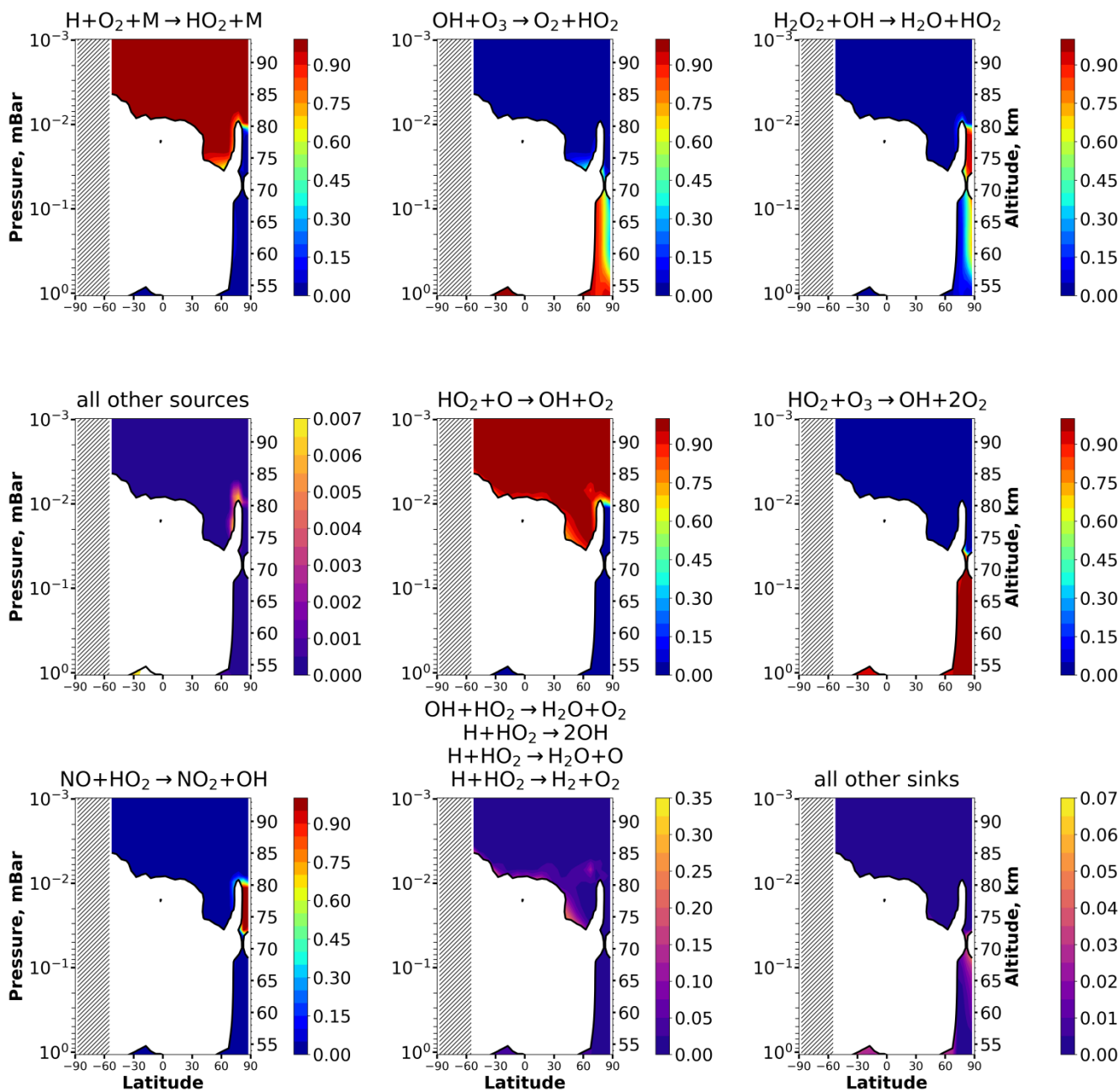
698



699

700 Figure 2. Nighttime mean and monthly averaged OH/OH^{eq} , where OH^{eq} is equilibrium concentration
 701 determined by Eq. (6). Black line shows the boundary of OH equilibrium according to condition (1). The
 702 stippling corresponds to $\chi < 105^\circ$. The white area represents the $\langle OH/OH^{eq} \rangle$ ratio outside the [0.5, 1.5]
 703 interval.

704

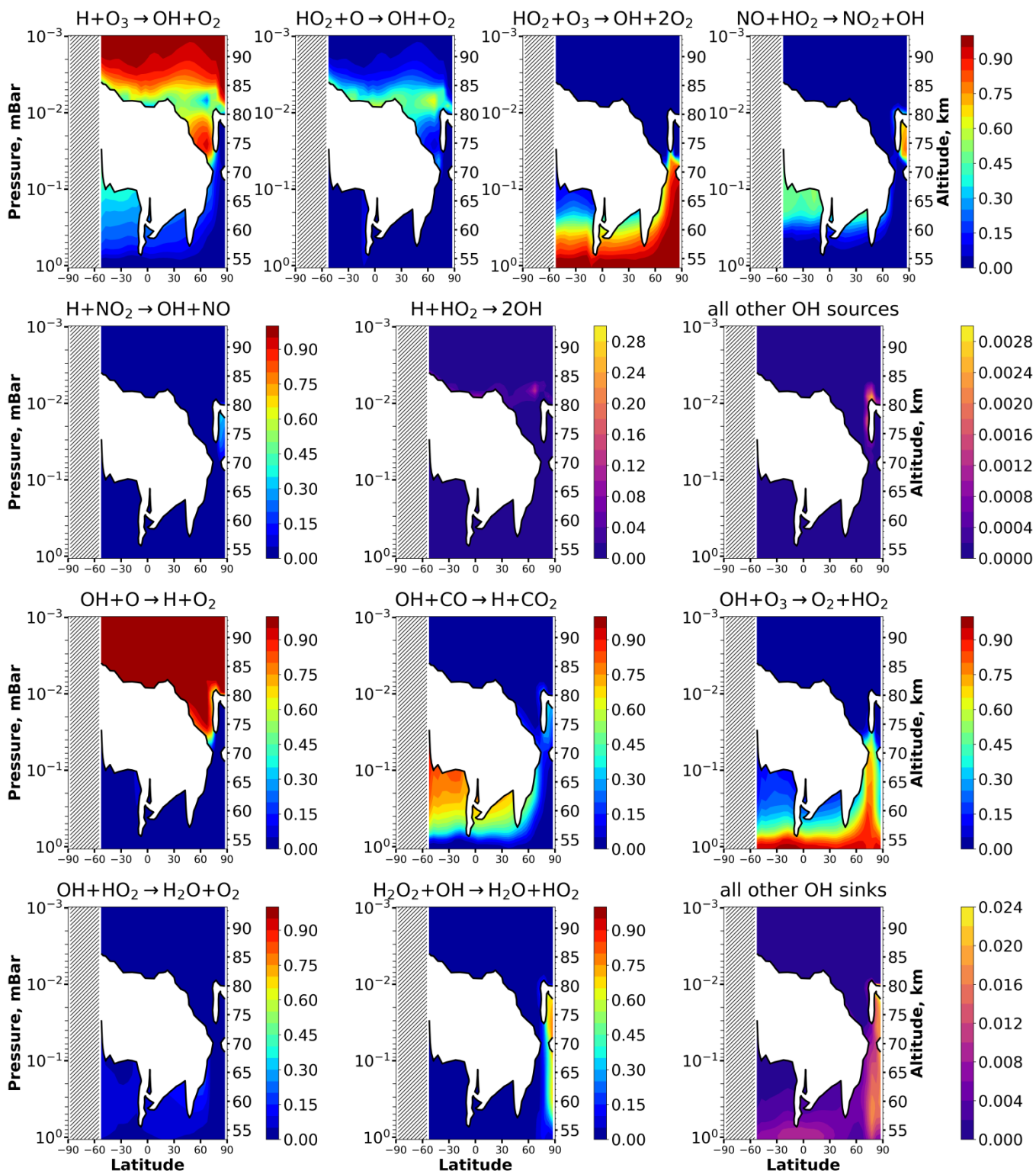


705

706

Figure 3. Nighttime mean and monthly averaged relative contribution of a certain reaction to the total source or sink of HO₂ in equilibrium areas. The stippling corresponds to $\chi < 105^\circ$. White color indicates nonequilibrium areas of HO₂.

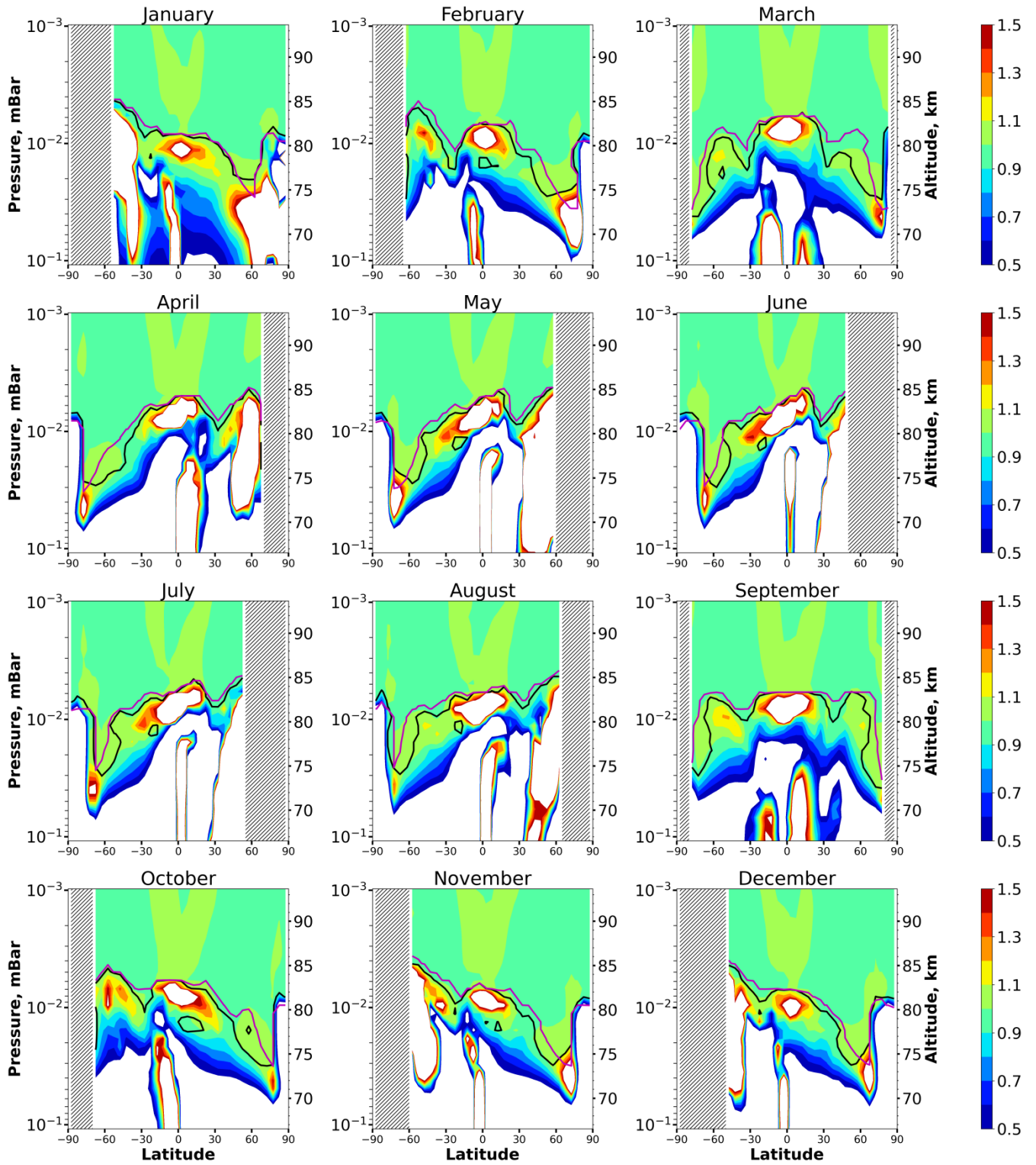
709



710

711 Figure 4. Nighttime mean and monthly averaged relative contribution of a certain reaction to the total
 712 source or sink of OH in equilibrium areas. The stippling corresponds to $\chi < 105^\circ$. White color indicates
 713 nonequilibrium areas of OH.

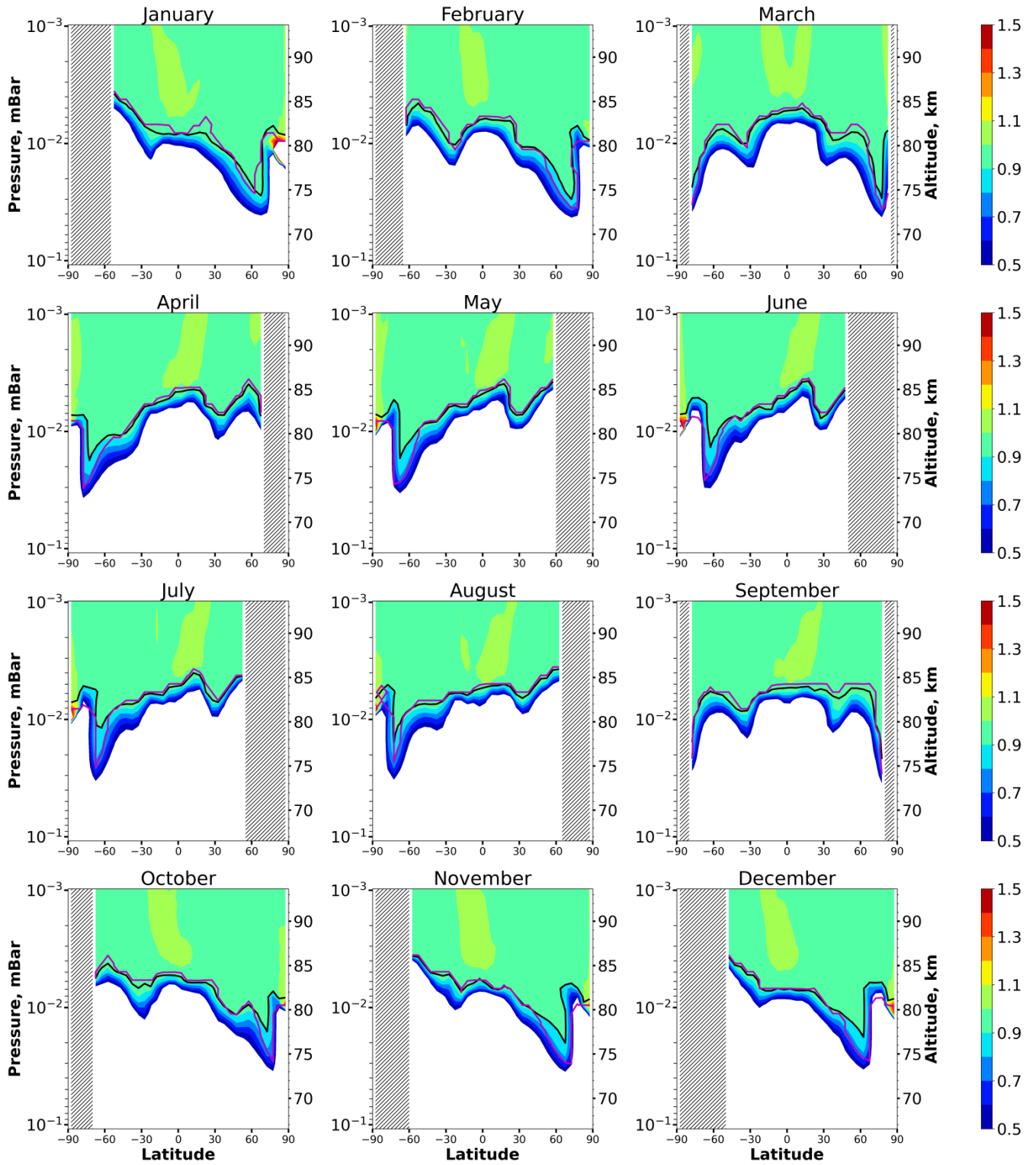
714



715

716 Figure 5. Nighttime mean and monthly averaged HO_2/HO_{2sh}^{eq} , where HO_{2sh}^{eq} is shortened equilibrium
 717 concentration determined by Eq. (9). Black line shows the boundary of HO_2 equilibrium according to
 718 condition (1). Magenta line shows $\langle Crit_{HO_2} \rangle = 0.1$. The stippling corresponds to $\chi < 105^\circ$. The white
 719 area represents the $\langle HO_2/HO_{2sh}^{eq} \rangle$ ratio outside the $[0.5, 1.5]$ interval.

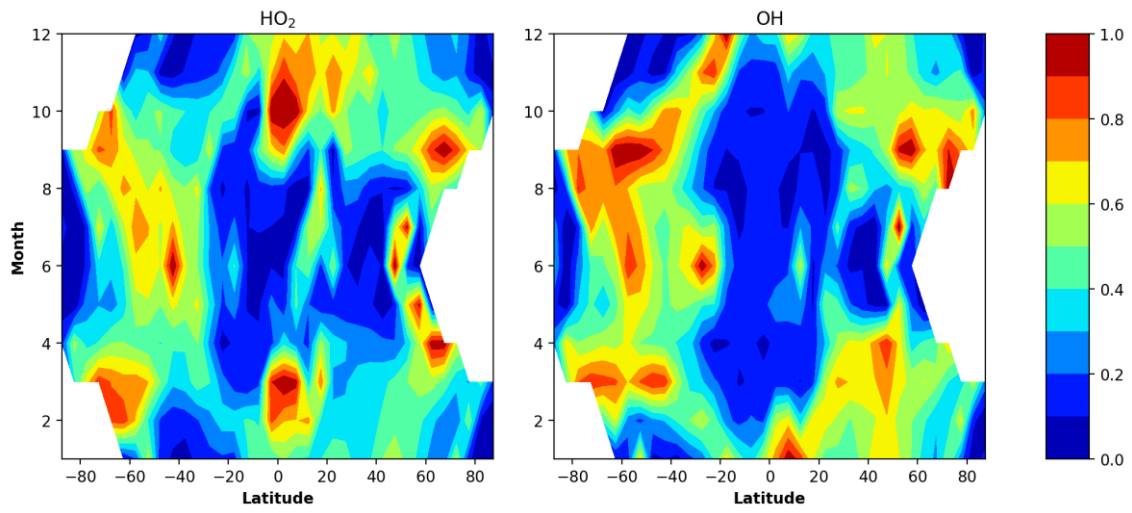
720



721

722 Figure 6. Nighttime mean and monthly averaged OH/OH_{sh}^{eq} , where OH_{sh}^{eq} is shortened equilibrium
 723 concentration determined by Eq. (10). Black line shows the boundary of OH equilibrium according to
 724 condition (1). Magenta line shows $\langle Crit_{OH} \rangle = 0.1$. The stippling corresponds to $\chi < 105^\circ$. The white
 725 area represents the $\langle OH/OH^{eq} \rangle$ ratio outside the $[0.5, 1.5]$ interval.

726



727

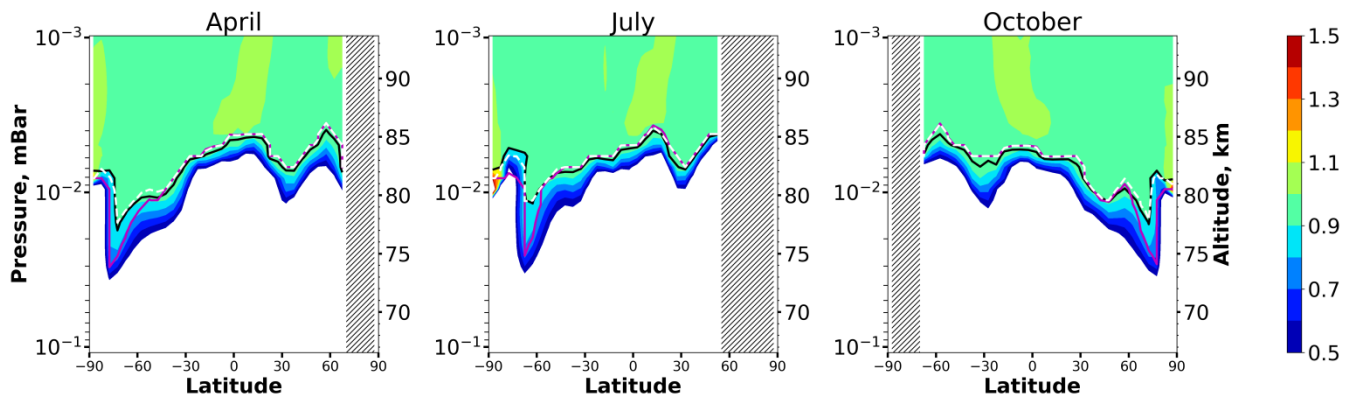
728

729

730

731

Figure 7. Monthly and longitudinally mean of total uncertainties in determination of the local heights of the OH and HO₂ equilibrium boundaries according to the criteria (17) and (25). The white color indicates the absence of data due to polar day.



732

733 Figure 8. Nighttime mean and monthly averaged OH/OH_{sh}^{eq} . Black line shows the boundary of OH
 734 equilibrium according to condition (1). Magenta line shows $\langle Crit_{OH} \rangle = 0.1$, dotted white line shows
 735 $\langle Crit_{OH}^m \rangle = 0.1$.

736